# THE RADIO PLASMA IMAGER INVESTIGATION ON THE IMAGE SPACECRAFT

B. W. REINISCH[1], D. M. HAINES[1], K. BIBL[1], G. CHENEY[1], I. A. GALKIN[1], X. HUANG[1], S. H. MYERS[1], G. S. SALES[1], R. F. BENSON[2], S. F. FUNG[2], J. L. GREEN[2], S. BOARDSEN[3], W. W. L. TAYLOR[3], J.-L. BOUGERET[4], R. MANNING[4], N. MEYER-VERNET[4], M. MONCUQUET[4], D. L. CARPENTER[5], D. L. GALLAGHER[6] P. REIFF[7]

[1]*University of Massachusetts, Center for Atmospheric Research, Lowell, MA 01854, U.S.A.*
[2]*NASA Goddard Space Flight Center, Greenbelt, MD, U.S.A.*
[3]*Raytheon ITSS, Goddard Space Flight Center, Greenbelt, MD, U.S.A.*
[4]*Observatoire de Paris, Meudon, France*
[5]*Stanford University, Stanford, CA, U.S.A.*
[6]*NASA Marshall Space Flight Center, Huntsville, AL, U.S.A.*
[7]*Rice University, Houston, TX, U.S.A.*

(Received May 10, 1999)

**Abstract.** Radio plasma imaging uses total reflection of electromagnetic waves from plasmas whose plasma frequencies equal the radio sounding frequency and whose electron density gradients are parallel to the wave normals. The Radio Plasma Imager (RPI) has two orthogonal 500-m long dipole antennas in the spin plane for near omni-directional transmission. The third antenna is a 20-m dipole along the spin axis. Echoes from the magnetopause, plasmasphere and cusp will be received with the three orthogonal antennas, allowing the determination of their angle-of-arrival. Thus it will be possible to create image fragments of the reflecting density structures. The instrument can execute a large variety of programmable measuring options at frequencies between 3 kHz and 3 MHz. Tuning of the transmit antennas provides optimum power transfer from the 10 W transmitter to the antennas. The instrument can operate in three active sounding modes: (1) remote sounding to probe magnetospheric boundaries, (2) local (relaxation) sounding to probe the local plasma frequency and scalar magnetic field, and (3) whistler stimulation sounding. In addition, there is a passive mode to record natural emissions, and to determine the local electron density, the scalar magnetic field, and temperature by using a thermal noise spectroscopy technique.

## 1. Background and Objectives

*Background*. For the first time an active radio plasma imager (RPI) will operate in space when NASA's IMAGE satellite orbits Earth. Unlike the passive plasma wave instruments on other satellites, e.g., WIND (Bougeret et al., 1995) and POLAR (Gurnett et al., 1995), RPI will use *active* Doppler radar techniques for the remote sensing of plasma structures. These techniques are similar to the ones used by the Digisonde Portable Sounder (DPS), a modern groundbased ionosonde (Reinisch et al., 1997). In the frequency range from 3 kHz to 3 MHz, RPI will omni-directionally transmit 10 W radio wave pulses, and receive reflected echoes



*Space Science Reviews* **91:** 319–359, 2000.

on three orthogonal antennas. Echo reflections occur at plasma structures where the density gradients are parallel to the wave normals of the incident waves, and where the wave frequency equals the plasma cut-off frequencies for either characteristic mode. The transmitted signals generally contain characteristic polarizations, the ionic or ordinary (O) mode, and the electronic or extraordinary (X) mode. These two modes give rise to two slightly displaced echoes from a given plasma structure. The O-echo is reflected when $N_{e(o)} = 0.0124\ \mathrm{f}^2$ (f in Hz, and electron number density $N_e$ in $\mathrm{m}^{-3}$), and the X-echo when $N_{e(x)} = 0.0124\ \mathrm{f}\ (\mathrm{f} - \mathrm{f_{He}})$ with $\mathrm{f_{He}}$ being the local electron gyrofrequency at the reflection point (Fung and Green, 1996; Davies, 1990, Ch. 4).

The highly eccentric IMAGE orbit will position the spacecraft for many hours near its apogee at a geocentric distance of 8 $R_{\mathrm{E}}$. In the magnetospheric cavity, $N_e$ is generally less than $10^6$ $\mathrm{m}^{-3}$, which means that the local plasma frequency $f_{pe}$ (Hz) $\approx 9\sqrt{N_e}$ is less than 9 kHz. Electromagnetic waves with frequencies $f > f_{pe}$ will propagate away from the spacecraft almost as in free space. Depending on the geometry of the magnetospheric boundaries with respect to the spacecraft location, RPI can 'see' several plasma structures simultaneously out to ranges of several $R_{\mathrm{E}}$.

*Objectives.* The scientific objectives of RPI include the detection of plasma influx into the magnetosphere during magnetic substorms and storms, and the assessment of the response of the magnetopause and plasmasphere to variations of the solar wind (Green et al., 2000; Green et al., 1998). Different measuring modes will be applied to achieve these objectives: pulsed sounding to measure remote plasma structures; relaxation sounding to measure the local electron density and magnetic field strength; thermal noise observations to measure the local electron density and temperature; high resolution natural emissions studies; and whistler studies to determine large scale plasma configurations.

*Instrument requirements*. The instrument requirements are controlled by the plasma densities and the dimensions of the magnetosphere that are illustrated in Figure 1. The frequency range from 3 kHz to 3 MHz covers plasma densities from about $10^5$ to $10^{11}$ $\mathrm{m}^{-3}$, designed to probe the magnetopause, plasmasphere, the cusp, and the top of the ionosphere. The maximum range from which echoes can be received is determined by the signal-to-noise ratio (SNR), as discussed in an earlier study on the feasibility of magnetospheric sounding (Calvert et al., 1995). To determine the dimensions and shape of the cavity between the magnetopause and plasmapause, RPI must 'illuminate' $4\pi$ steradians with pulsed radio signals and measure the echoes arriving from different directions. Quadrature sampling and Doppler analysis of the signals received on three orthogonal antennas can determine the angles-of-arrival of the echoes, their polarization ellipses and the Faraday rotation (Reinisch et al., 1999). The location of echo targets should be measured with an angular resolution of 2° and a range resolution of 0.1 $R_{\mathrm{E}}$. To correctly interpret the echoes in terms of the plasma characteristics of the reflector it is necessary to determine the wave polarizations of the echoes, i.e., the O- and X-wave components.

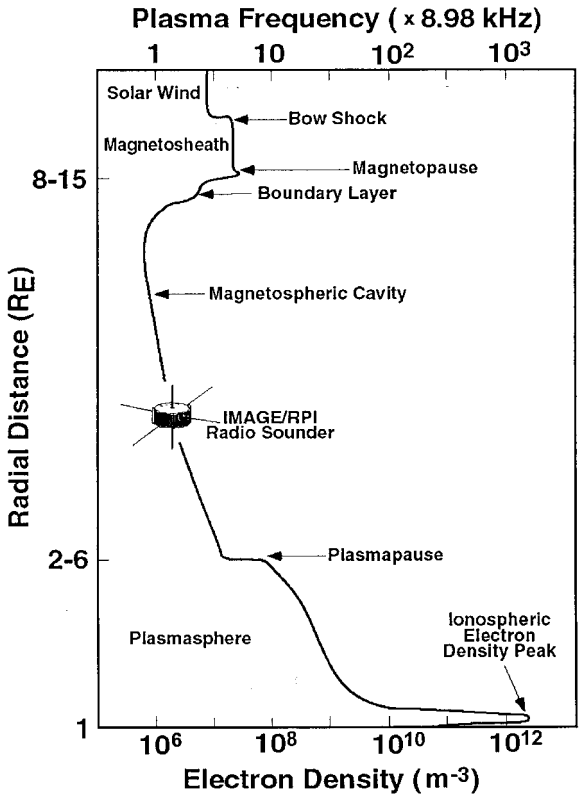


*Figure 1.* Electron density distribution vs. geocentric distance from the center of the earth in the direction of the Sun (after Green et al., 1998).

## 2. Theoretical Basis of RPI Measurements

### 2.1. RPI SOUNDING AND IMAGING

In this mode, RPI transmits a sequence of narrow radio pulses (nominally 3.2 ms) at each sounding frequency and measures echoes returning in the time between transmit pulses.

*Antenna coordinate system.* The three orthogonal antennas define the reference coordinate system $xyz$ for all RPI measurements as shown in Figure 2. The radio wave is described in the primed coordinate system $x'y'z'$ (Figure 3(a)). When an echo arrives along the $z'$-axis, RPI must determine the polar and azimuth angles, $\theta$ and $\phi$. In the $xyz$ system, the received $E_R$ vector of the arriving echo signal can be written as:

$$\mathbf{E}_R(t) = (E_{Rx}\mathbf{x} + E_{Ry}\mathbf{y} + E_{Rz}\mathbf{z})e^{i\omega t} \tag{1a}$$

or

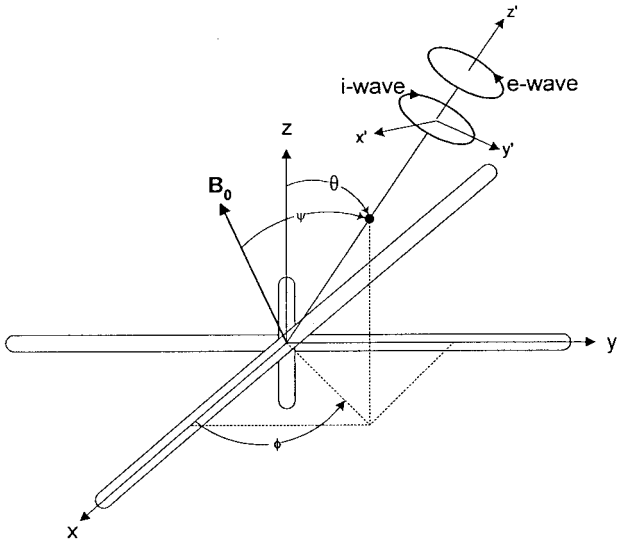


*Figure 2.* The antenna coordinate system $xyz$.

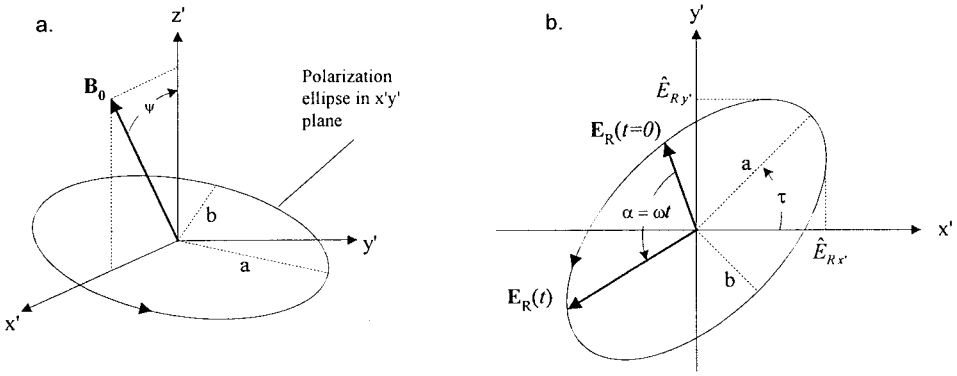


*Figure 3.* The polarization ellipse in the $x'y'$ plane for a wave propagating along the $z'$ axis. (a) The orientation of the $x'y'z'$ system with respect to the magnetic field $B_0$. (b) The tilt angle $\tau$ of the polarization ellipse; $a$ and $b$ are the semimajor and minor axes. The sense of rotation of the $E_R$ vector assumes an extraordinary wave.

$$\mathbf{E}_R(t) = (\hat{E}_{Rx}e^{i\alpha_x}\mathbf{x} + \hat{E}_{Ry}e^{i\alpha_y}\mathbf{y} + \hat{E}_{Rz}e^{i\alpha_z}\mathbf{z})epi\omega t \ , \tag{1b}$$

where $\alpha_m$ is the phase associated with each field component.

In the $x'y'z'$ system (Figure 3(b)) the field can be expressed as:

$$\mathbf{E}_R(t) = (\hat{E}_{R\mathbf{x}'}\mathbf{x}' + E_{Ry'}\mathbf{y}')e^{i\omega t} \tag{1c}$$

or

$$\mathbf{E}_R(t) = (\hat{E}_{Rx'}e^{i\alpha_{x'}}\mathbf{x}' + \hat{E}_{Ry'}e^{i\alpha_{y'}}\mathbf{y}')e^{i\omega t} \ . \tag{1d}$$

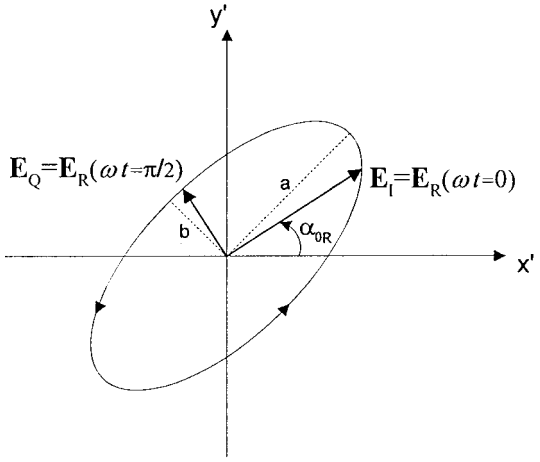


*Figure 4.* The normal to the polarization plane expressed in terms of the quadrature field vectors. The direction of the normal is controlled by the sense of rotation of the $\mathbf{E}_R$ vector. It points in the direction of the wave vector for right hand polarization with respect to the wave vector **k** (shown here), otherwise it points opposite to **k**. This ambiguity can be resolved with the help of the signatures in a given plasmagram and the use of models for the magnetopause and plasmapause (see Section 5.2).

In this paper, the lower case is used for unit vectors, and the Ê's are the component peak amplitudes (Figure 3(b)). Each field component in (1a) produces its corresponding receiver output voltage $V_m$ where $m = x$, $y$, and $z$. The final intermediate frequency (IF) signals at each of the three receiver outputs is digitized at 1.6 ms intervals. For RPI, IF = 45 kHz, i.e., the IF is much larger than the signal bandwidth which is limited by the 300 Hz receiver bandwidth. It is therefore possible to obtain the amplitude and phase of each antenna signal from two quadrature voltage samples $I_m$ and $Q_m$ that are offset in time by a quarter IF cycle. When the radio frequency (RF) signal is mixed with the local oscillator signal, the RF phase $\alpha_{0R}$ (see Figure 4) is conserved. This is the same technique that the groundbased Digisondes successfully used for many years (Bibl and Reinisch, 1978) with IF = 225 kHz and a receiver bandwidth of 15 kHz. The *voltage vector:*

$$\mathbf{V}(t) = (V_x\mathbf{x} + V_y\mathbf{y} + V_z\mathbf{z})e^{i\omega t} \tag{2}$$

is therefore proportional to the $\mathbf{E}_R$ vector, i.e., $\mathbf{V} = \Gamma\mathbf{E}_R$. The proportionality factor $\Gamma$ is the product of the effective antenna length $L' \approx 0.5L_a$, where $L_a$ is the tip-to-tip dipole length, and the receiver voltage gain $G$. For RPI, $L'_{x,y} \approx 250$ m , $L'_z \approx 10$ m, and the nominal receiver gains are $G_{x,y} = 10^3$ and $G_z = 25 \times 10^3$, i.e., $\Gamma = 2.5 \times 10^5$. The vector components in (2) are:

$$V_x(t) = \hat{V}_x e^{i(\omega t+\alpha_x)}, \quad \hat{V}_y(t) = \hat{V}_y e^{i(\omega t+\alpha_y)}, \quad V_z(t) = V_z e^{i(\omega t+\alpha_z)}\ , \tag{3a}$$

It follows that the digital samples taken at $\omega t = 0$ and $\omega t = \pi/2$, i.e., the quadrature voltage samples $I_m$ and $Q_m$, are:

$$I_m = \hat{V}_m e^{i\alpha_m}, \quad Q_m = \hat{V}_m e^{i(\alpha_m + (\pi/2))}, \quad m = x, y, z \tag{3b}$$

and

$$\hat{V}_m = \sqrt{I_m^2 + Q_m^2}, \quad \alpha_m = \tan^{-1} \frac{Q_m}{I_m} . \tag{3c}$$

*Echo angle-of-arrival.* The *quadrature vectors* $\mathbf{I} = (I_x, I_y, I_z)$ and $\mathbf{Q} = (Q_x, Q_y, Q_z)$ defined in (3b) are proportional to the field vectors $\mathbf{E}_I$ and $\mathbf{E}_Q$ at $\omega t = 0$ and $\pi/2$ respectively (Figure 4). They can therefore be used to calculate the normal to the wave front. It is a standard technique to calculate the normal to a plane by forming the vector product of two vectors lying in the plane (Shawhan, 1970; Reinisch et al., 1999). The normal **n** is therefore given by (Figure 4):

$$\mathbf{n} = \frac{\mathbf{E}_1 \times \mathbf{E}_Q}{|\mathbf{E}_I \times \mathbf{E}_Q|} = \frac{\mathbf{I} \times \mathbf{Q}}{|\mathbf{I} \times \mathbf{Q}|} = \frac{\mathbf{I} \times \mathbf{Q}}{I\,Q} . \tag{4}$$

The direction of the normal is controlled by the sense of rotation of the $\mathbf{E}_R$ vector. It points in the direction of the wave vector for right-hand polarization with respect to the wave vector **k** (as shown in Figure 4), otherwise it points opposite to **k**. This ambiguity can be resolved with the help of the signatures in a given plasmagram and the use of models for the magnetopause and plasmapause (see Section 5.2). The angles $\theta$ and $\phi$ for the $z'$-axis can be obtained from:

$$n_x = \sin\theta \cos\phi, \quad n_y = \sin\theta \sin\phi, \quad n_z = \cos\theta . \tag{5}$$

We have shown in a feasibility paper (Calvert et al., 1995) that the expected angular resolution of an instrument like the RPI is about 1°, depending on the SNR. It must be realized that the angle-of-arrival can only be measured with the above-described procedure if a single echo of frequency, $f$, arrives at the spacecraft at a given time. To achieve this condition for the majority of echoes, the transmitted RPI signal has a 3.2 ms pulse width thus limiting time-coincident echoes to targets whose virtual ranges are within 480 km of each other. In addition, RPI uses Fourier analysis on all signals to separate time-coincident echoes by making use of the direction-dependent Doppler shifts. It is considered very unlikely that echoes from different directions which happen to have the same propagation delay also have the same Doppler shift $d = \mathbf{k} \cdot (\mathbf{v} - \mathbf{v}_S)/\pi$ (Reinisch et al., 1987), where **v** is the target velocity, and $\mathbf{v}_S$ the spacecraft velocity. This echo source identification technique, using Doppler analysis and direction finding, had been pioneered for radio sounding from the ground by Bibl and Reinisch (1978).

*Radio imaging.* Once the range and angle-of-arrival of all echoes with an adequate SNR are determined it is possible to construct a partial image of the plasma distribution. To simulate the effect of noise on the accuracy of the angular measurements, we calculated the receiver output voltages for a signal with field strength $E_R$ arriving at angle $(\theta, \phi)$. A random noise voltage $V_N$ was added to the signal voltages and the angle-of-arrival was calculated from (4) and (5). This process was repeated 100 times with the noise voltage varying uniformly from $-1.732(E_R/\mathrm{SNR})$

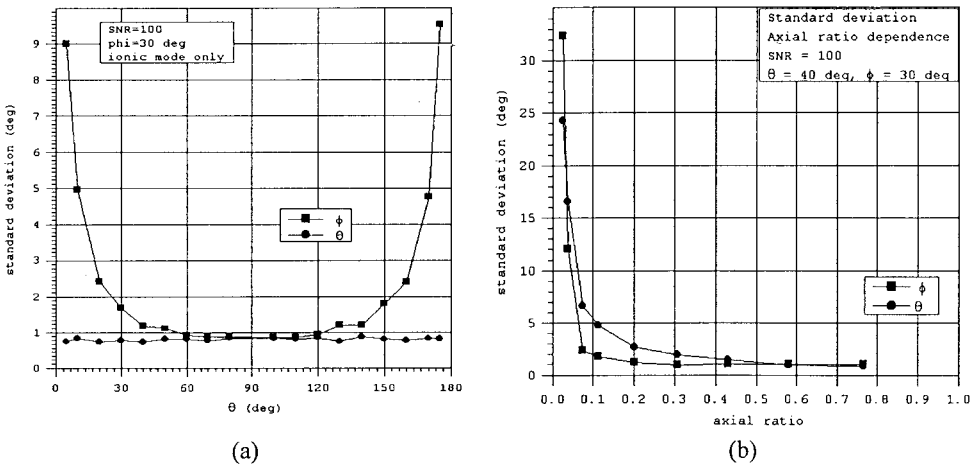


*Figure 5.* Standard deviation of the angle-of-arrival for SNR $= 100$, (a) as function of $\theta$ for an elliptical O-wave, (b) as function of axial ratio $\rho$ for a fixed arrival angle.

to $+1.732(E_R/\text{SNR})$ (Hald, 1962, Ch. 5). Figure 5(a) shows the standard deviation for $\theta$ and $\phi$ as function of the polar angle $\theta$ for SNR $= 100$ and $\phi = 30°$. In this simulation, an ordinary mode elliptically polarized signal was assumed. The standard deviation is typically slightly less than 1° for the assumed SNR and increases proportionately to the inverse of the SNR. For $\theta$ close to 0° and 180°, i.e., only at the poles, the standard deviation of $\phi$ becomes large. To check the effect of the wave polarization on the angle measurements, the axial ratio of the polarization ellipse was changed from $\rho = 1$ (circular) to $\rho = 0$ (linear). Figure 5(b) shows that the angle-of-arrival cannot be found with the technique described here for a linearly polarized wave. Fortunately, this is not a serious limitation since Reinisch et al. (1999) have shown (Figure 4) that the angle between $\mathbf{B}_0$ and the wave vector $\mathbf{k}$ must be $90° \pm 1°$ for the characteristic waves to have an axial ratio of $\rho < 0.1$. This means that RPI cannot determine the arrival angles of linearly polarized signals which arrive from a direction perpendicular to the local magnetic field direction, unless the magnetic field direction is precisely known. In that case the polarization measurement determines the arrival angle.

The measured echo locations for each sounding frequency allows us to determine the configuration of the corresponding plasma. Using ray-tracing techniques, one can then adjust the models of the density distribution until they reproduce the observed reflection points. As an initial step in the analysis, the echoes will be displayed on *echo-maps* as described in Section 5.

### 2.2. *IN SITU* PLASMA MEASUREMENTS FROM QUASI-THERMAL NOISE SPECTROSCOPY

In addition to the radio imaging, RPI will perform *in situ* measurements of the electron density and temperature using quasi-thermal noise spectroscopy. These *passive* measurements of the ambient electric field as a function of frequency near the electron plasma frequency are complementary to *active* radio sounding since the passive measurements are of the local environment and the active measurements are of the global environment. This allows the study of global and local processes and their interdependence.

*Basics of the thermal noise spectroscopy technique.* In a stable plasma, the thermal motion of particles produces electrostatic fluctuations, which are completely determined by the plasma density and velocity. Hence this quasi-thermal noise, which will be measured with the sensitive RPI receivers at the terminals of the three electric antennas, will allow *in situ* plasma measurements. The method is especially adapted to measure the electron density and thermal temperature, which are revealed by the noise spectrum around the plasma frequency, and can also give diagnostics of supra-thermal electron parameters (Meyer-Vernet and Perche, 1989), and of the plasma bulk speed (Issautier et al., 1999). The frequency just below the peak of the electric field spectrum is the plasma frequency of the surrounding plasma, allowing the local electron plasma density to be determined. The spread of the peak is a measure of the electron plasma temperature and the fine structure near the peak allows characterization of the distribution of the supra-thermal electrons.

When the electron gyrofrequency, $f_{\mathrm{He}}$, is sufficiently smaller than the electron plasma frequency, $f_{pe}$, the electron thermal motions excite Langmuir waves, so that the quasi-equilibrium spectrum has a low frequency cut-off at $f_{pe}$, with a peak just above it (see Section 5). In addition, the electrons passing the antenna at a distance closer than a Debye length will induce voltage pulses on it, producing a plateau in the wave spectrum below $f_{pe}$ and a decreasing level above $f_{pe}$. Since the Debye length is primarily determined by the thermal electrons, the peak of the spectrum is determined by the plasma frequency, and the plateau is determined by the thermal electrons. In contrast, since the Langmuir wave phase velocity becomes very large near $f_{pe}$, the fine structure of the peak is determined by the supra-thermal electrons.

This technique has been used to determine the plasma characteristics of a number of space plasma environments and as a reference measurement for other techniques (Meyer-Vernet et al., 1998). It has recently been used in Earth's plasmasphere on Wind (Moncuquet et al., 1995) and on AMPTE (Lund et al., 1995). Because the technique relies on a wave measurement, which senses a large plasma volume with a characteristic size of the order of the antenna length, it is relatively immune to the spacecraft potential and photoelectron perturbations. These perturbations are confined to a region with a characteristic dimension of the Debye length around the spacecraft. These spacecraft potential and photoelectron perturbations do adversely affect measurements by particle analyzers and Langmuir

probes. In a warm plasma when $f_{\mathrm{He}}$ is not small compared to $f_{pe}$, the electron thermal motion excites Bernstein waves. The observed plasma noise spectrum in this case has weak peaks in the amplitude spectrum with well-defined minima at gyroharmonics, which, from their spacing, allows an independent measurement of the absolute value of the magnetic field (Meyer-Vernet et al., 1993). These field strength measurements can be compared with the results from active or relaxation sounding.

*Implementation in RPI.* The frequency of the peak in the electric field spectrum is very easy to locate and is nearly independent of gain calibrations. The main limitations of the technique are the Debye length and the presence of other sources of noise. When the Debye length increases and approaches the antenna length, the antenna becomes less adapted to measure the Langmuir waves and the peak broadens so that both the density and temperature become difficult to measure accurately. Therefore, for accurate measurements, the antenna length must be significantly larger than the local Debye length. Because of this limitation, different antennas will be used in different parts of the orbit. The short, 20-m antenna, which is best suited to rather dense and cold plasmas, will be used to measure the ambient plasma in the plasmasphere and plasmapause, whereas the long, 500-m antenna will be used in the less dense and hotter magnetospheric cavity. The RPI is particularly well designed to make these measurements since it will be able to measure the electron density and temperature over a range of several decades.

### 2.3. WHISTLER-MODE STUDIES WITH RPI

*Basic considerations.* Within the plasmasphere and at low altitudes over the southern polar region the lower frequencies of the RPI may be used for transmission and reception in the whistler mode. This mode exists for frequencies lower than the smaller of the electron plasma and gyrofrequency, $f_{pe}$ and $f_{\mathrm{He}}$. The whistler mode frequencies will often be in the range 3–30 kHz but may occasionally reach up to several hundred kHz. Under many conditions the local refractive index will become large, of order 10. Propagation velocities will then be low, of order $c/10$, so that pulse travel times over path segments several Earth radii in length will be of order 1–2 s. Near half the local electron gyrofrequency, the 500-m RPI antennas will approach a half wave length and should be quite efficient, capable of radiating approximately 1 W of whistler-mode power.

Whistler-mode operations by RPI will allow (1) a study of the properties of an electric antenna operated in the magnetospheric plasma at whistler mode frequencies, (2) investigation of the distribution of plasma along geomagnetic field lines, (3) study of large and small scale plasma density structures and their influence on the propagation of whistler mode waves, including mode conversion between electrostatic and electromagnetic waves at sharp boundaries and in regions of small scale plasma irregularities, (4) investigation of the growth of whistler mode waves

due to interactions with the energetic electron population of the magnetosphere, and (5) study of downward ionospheric penetration by whistler mode signals.

*Implementation in RPI.* The experiments will in several ways be analogous to those conducted in the conventional free-space sounding mode. In principle, transmitted signals should spread widely in the medium and undergo reflections at distant points. Some of these reflected rays return to the satellite. Some signals may penetrate to the ground during special geophysical conditions. On IMAGE the signal levels of the returning signals may vary widely with respect to the noise level both in space and time. The properties of returning signals such as group delay, wave normal angle, and amplitude spectrum will provide information on the propagation paths that have been followed and on the extent to which significant wave particle interactions have occurred. If another satellite with a suitable whistler-mode receiver is available near the longitude of RPI, there is a high probability of successful receptions on that satellite over a wide range of latitudes.

## 3. The RPI Instrumentation

### 3.1. System description and configuration

*System description.* Table I gives a summary of the instrument characteristics. Since RPI is a radar, most of the critical design parameters, which characterize RPI's capabilities and performance, are typical radar system performance parameters:

- Detection range: the maximum range at which objects/ structures can be observed. For a plasma sounder, it is the maximum virtual range $R' = 0.5ct_e$.
- Unambiguous range: the range beyond which an object reappears at an apparent closer range.
- Range resolution: the minimum separation distance at which multiple objects can be distinguished.
- Frequency band: the range of frequencies from the lowest to the highest sounding frequency.

*System configuration.* Figure 6 shows the configuration of RPI's components and assemblies, including:

- Four 250 m wire antennas (0.4 mm diameter) along the $x$ and $y$-axes in the satellite spin-plane (Figure 2); used for transmission and reception.
- Two 10 m wire (0.4 mm diameter) antennas deployed along the spin axis ($z$-axis), and supported by a self-erecting lattice boom; used for reception only.
- RPI Electronics, containing two transmitter exciters, three receivers, and digital control and power circuits.
- Four antenna interface units for the spin-plane antennas, each containing a 250-m wire-antenna deployer and another smaller housing containing an RF transmitter, a CPU switched antenna matching network (coupler), and a receiver preamplifier.
- Two preamplifiers for the 10-m wire-antennas supported by the $z$-axis booms.

TABLE I
RPI operational characteristics

| System parameter | Nominal | Limits | Rationale |
|---|---|---|---|
| Radiated power | 10 W @ 5% to 20% duty cycle | 10 W per antenna element | Required for adequate SNR |
| Frequency range | 3 kHz–3 MHz | | Covers expected range of plasma densities. |
| Freq. accuracy | $1 \times 10^{-5}$ | | Accurately measures observed plasma densities |
| Freq. steps | 5% steps | 100 Hz | 5% in frequency gives 10% in plasma density resolution. |
| Measurement duration | 1 s to $\sim$ min | 50 ms | Different spatial and temporal requirements along orbit |
| Maximum virtual range | 120 000 km | 300 000 km | Extent of expected magnetospheric echoes |
| Minimum virtual range | 980 km w. 3.2 ms short pulses | 0 km for passive modes | Pulse width + receiver recovery time is 6.4 ms |
| Range increments | 240 km | 240 or 480 km | Required sampling resolution |
| Pulse rep rate | 1 $s^{-1}$ | 0.5 to 20 $s^{-1}$ | Sets unambiguous range |
| Pulse width | 3.2 ms | 3.2 ms to 1.9 s | Provide 480 km range resolution |
| Receiver bandwidth | 312 Hz | | Consistent with 3.2 ms pulse width |
| Receiver sensitivity | 25 nV/$\sqrt{\text{Hz}}$ (X&Y) 8nV/$\sqrt{\text{Hz}}$ (Z) | | Keeps receiver noise below cosmic noise |
| Coherent integration time | 8 s | 125 ms to 64 s | Provides both processing gain and Doppler resolution |
| Doppler resolution | 125 mHz | | Determined by coherent integration time |
| Receiver saturation recovery | 6 ms | | Specially designed monostatic radar receiver |
| Doppler range | $\pm$2 Hz | $\pm$150 Hz | To measure expected plasma velocities |
| Amplitude resolution | 3 dB | 3/8 dB | Data format allows 3/8 dB, but typical display is 3 dB |
| Angle-of-arrival resolution | 1° | 1° when SNR is 40 dB or better | Identify echo direction with required accuracy |
| Antenna length | 10 m & 250 m | | SNR required |
| Processing gain | 21 dB | 0 to 33 dB | To enhance weak echoes |

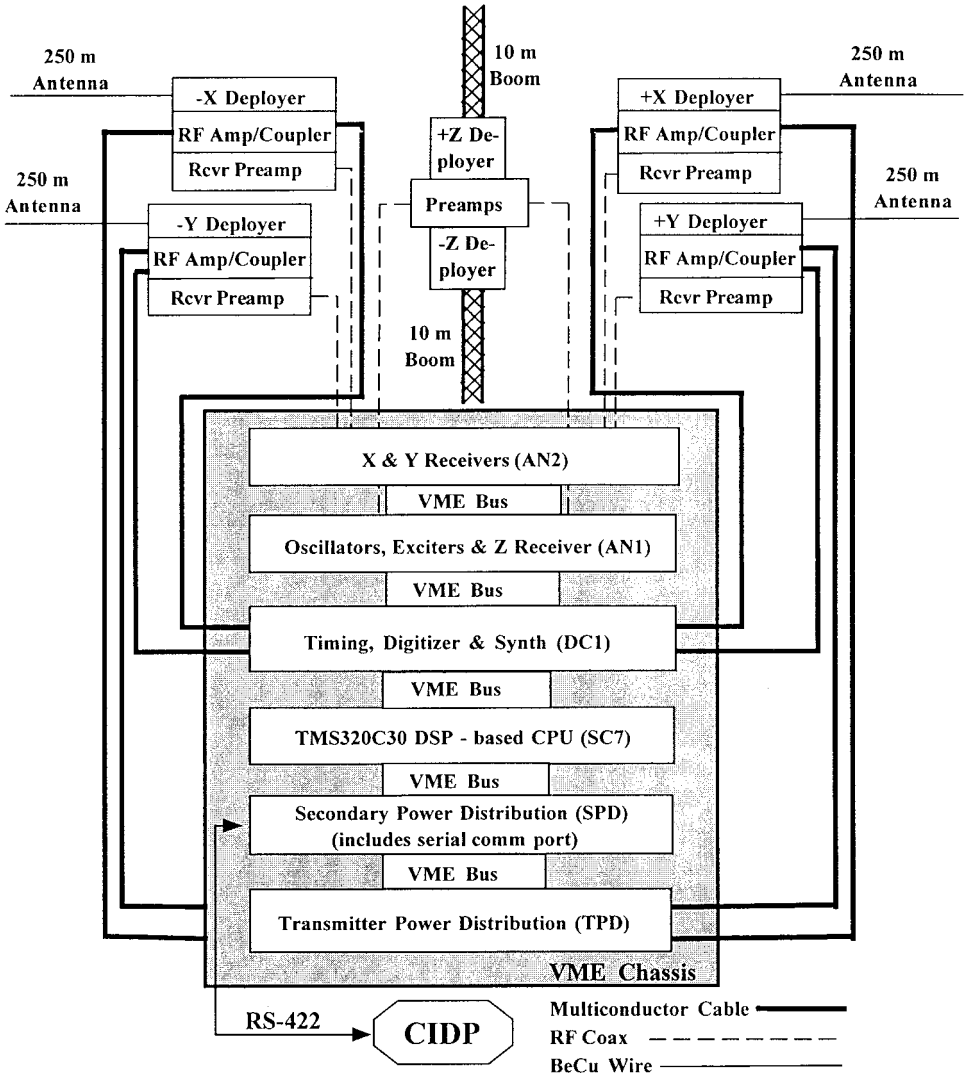


*Figure 6.* RPI Electronics Chassis and the interface to the antennas. The Common Instrument Data Processor (CDIP) controls and services all science instruments onboard IMAGE, handles RPI's power, and controls deployment of the antennas. It also buffers the data output from RPI and provides the telemetry interface.

### 3.2. RPI CONTROL UNIT

The SC7 CPU executes active and passive measurement sequences by writing digital bytes to the other boards via the VME interface. Power to the RPI is controlled and conditioned by the Common Instrument Data Processor (CIDP) to avoid voltage or current overloads. In addition, 'pass-through' commands from the ground, commands autonomously generated by the CIDP, and time and position updates

arrive via a serial communications line from the CIDP. Completed science data or system status telemetry packets are transferred to the CIDP for storage and relay to the ground.

*SC7 CPU board.* The SC7 is a VME compatible, 6-U form factor, computer board built by Southwest Research Institute. It is based on a Texas Instruments TMS320C30 floating point digital signal processor (DSP) chip. A single 2 kbyte bank of PROM stores the bootstrap loader program. Two 256 kbyte EEPROMs store RPI's operating software including the measurement programs and schedules. For redundancy purposes the two chips contain identical copies of all software. When a new block of operating software is uploaded, the block length is recorded at the beginning of each block, and a checksum is stored at the end. This enables the CPU, operating from the bootstrap loader program stored in the PROM, to check the integrity of stored data before loading and executing any software.

Figure 7 shows the control interface between the CIDP and the RPI circuit boards. The SC7 connects to the RPI boards via the VME bus. An RS-232 interface is available to connect ground support equipment (GSE) during ground testing. The RPI timing module on the Digital Card (DC1), generates an interrupt pulse every 1.6 ms. The timing waveforms are phased such that all actions necessary to control the hardware for each transmitted pulse can be taken in response to this hardware interrupt. The controllable system parameters which can be set during this interrupt are: waveform selection; receiver gain; receiver operating frequency; receiver pre-selector frequency; antenna coupler setting; X and Y transmitter enabling; transmitter power level; system high/low/standby power level; digitizer channels (built-in-test or receiver sampling).

### 3.3. TRANSMITTERS AND ANTENNAS

*Antenna system.* RPI uses three orthogonal dipoles, one 20 m tip-to-tip dipole, for reception only, along the spin axis of the spacecraft, and two 500 m tip-to-tip orthogonal spin plane dipoles that are used for transmission and reception. An important part of the RPI development effort was the design of the transmitter and the transmit antenna system to efficiently radiate enough power to provide detectable echoes at long ranges. For a fixed, higher frequency the antenna design would be trivial because we could use a half-wave dipole that would be resonant at the operating frequency. This procedure is not possible for RPI because the same antenna length is used to cover a ten-octave frequency band. The primary operational range for magnetospheric sounding is 10 kHz to 300 kHz, corresponding to wavelengths from 30 km to 1 km, so antenna lengths of several kilometers would be ideal. The RPI transmit antennas were made as long as was considered technically feasible, using four monopole elements of 250 m each. They are resonant half-wavelength dipoles at close to 300 kHz (Figure 8). Over a large portion of the primary frequency range, however, the 500-m dipole is an electrically short antenna.

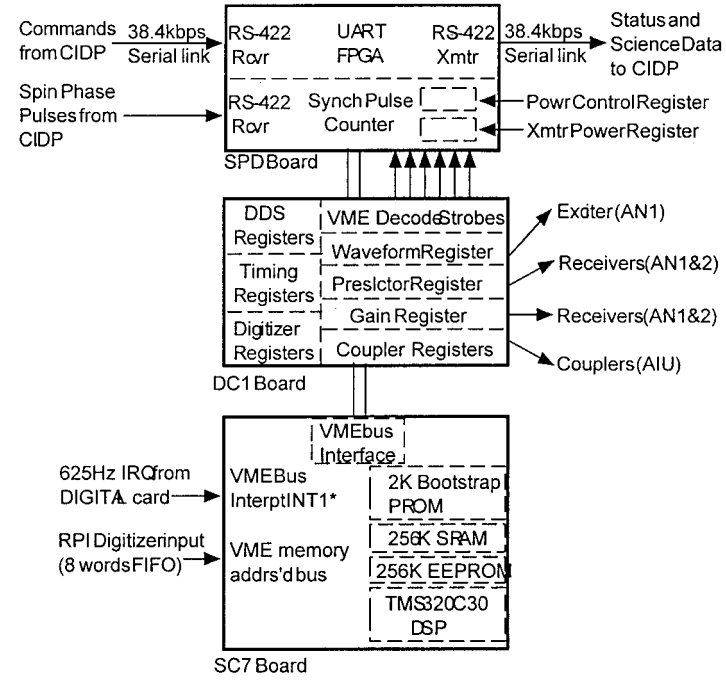


System Component Abbreviations:

AN1 - Analog I, 6U VME card
AN2 - Analog II, 6U VME card
AIUs - Antenna Interface Units - Assembly located at near each spin plane antenna, containing RF Amp, Antenna Coupler, Preamp & T/R switch
CIDP - Common Instrument Data Processor
DC1 - Digital Card 1, 6U VME card
FPGA - Field Programmable Gate Array
IRQ - Interrupt Request
SC7 - 'C30 CPU, 6U VME card
SPD - Secondary Power Distribution, 6U VME card
TPD - Transmitter Power Distribution, 6U VME card
UART - Universal Asynchronous Rcvr/Xmtr (parallel/serial converter)

*Figure 7.* SC7 internal and external interfaces.

The three thin-wire dipole antennas and their deployers have been designed and built by AEC (Able Engineering Company). The antenna material is 7-strand BeCu wire with a diameter of 0.4 mm. The IMAGE spacecraft will have a spin rate of 0.5 rotations per minute (rpm). This spin rate is sufficient to keep the two 500-m dipoles with their tip masses of 50 g in stable positions. A thin-wire antenna is also required for the dipole along the spin axis in order to minimize the photo-electric noise (Meyer-Vernet et al., 1998) that could affect the quasi-thermal noise spectroscopy measurements. Two self-erecting fiberglass lattice booms extend the two 10-m wires to their measurement positions.

*Transmitting on electrically short dipoles.* There are two challenges to transmit on an electrically short dipole. First, for $f < 300$ kHz, the antenna impedance is mainly capacitive with a reactance of $X_a = 1/\omega C$ where the capacitance, $C$,

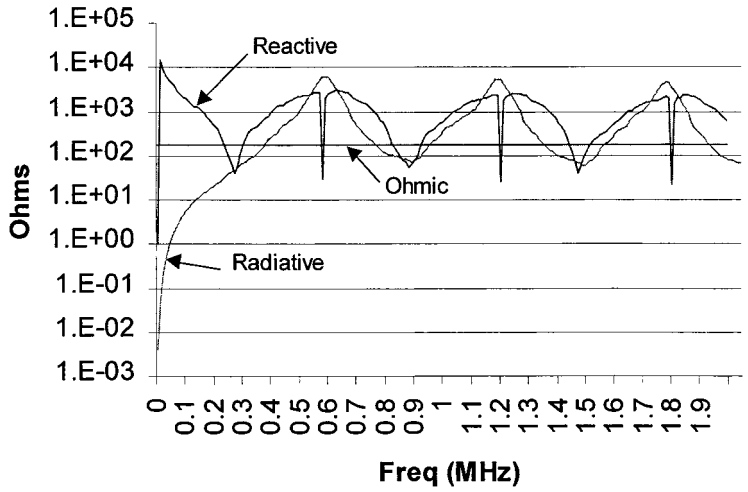


*Figure 8.* Reactance and resistance of a 500-m dipole.

of the 500-m dipole is 533 pF. A very high voltage is therefore required to drive a sufficiently high current $I_a$ into the antenna. Secondly, the radiation efficiency is very poor at low frequencies. If $R_r$ is the radiation loss resistance, the radiated power is $P_r = I_a^2 R_r$. For a short thin-wire dipole the radiation resistance $R_r = 20\pi^2 (L/\lambda)^2$ (Kraus, 1988, Ch. 5) where $L = 500$ m for RPI and $\lambda$ is the wavelength. Figure 8 illustrates the large variation of the magnitude of the reactance, $|X_a|$, and of the radiation resistance, $R_r$, with frequency. Starting with 10 mΩ at 10 kHz, $R_r$ increases to 73 Ω at resonance (∼300 kHz) and to 8 kΩ at anti-resonance (∼600 kHz). The total resistance $R_a$ (Figure 9) of the dipole is the sum of $R_r$ and the ohmic loss resistance $R_s \approx 180$ Ω (Figure 8). Clearly, the capacitive reactance dominates below 200 kHz and determines how much current flows into the antenna. For safety reasons, we have limited the voltage between the antenna and the spacecraft skin to 1.5 $kV_{rms}$ (or $V_a = 3$ $kV_{rms}$ between the antenna terminals). This limitation allows components rated at 5 kV to be safely used. Antenna tuning in the coupler is used to generate the required high voltages and is discussed in the next section.

Transmission with a single dipole would result in a doughnut-shaped radiation pattern (proportional to $\sin^2 \beta$ where $\beta$ is the direction with respect to the dipole axis). To fill in the pattern nulls, RPI will transmit on two orthogonal dipoles driven in phase quadrature (90° out of phase). The resulting power radiation pattern, proportional to $(1 + \cos^2 \theta)$ where $\theta$ is the angle with respect to the $z$-axis, is nearly isotropic with $I_a^2 R_r$ in the antenna plane, and $2I_a^2 R_r$ normal to this plane (Reinisch et al., 1999).

*Antenna couplers*. Each monopole has its own amplifier/antenna coupler (Figure 10). Direct application of a switched high voltage would consume too much current since it would require charging and discharging of the antenna capacitance

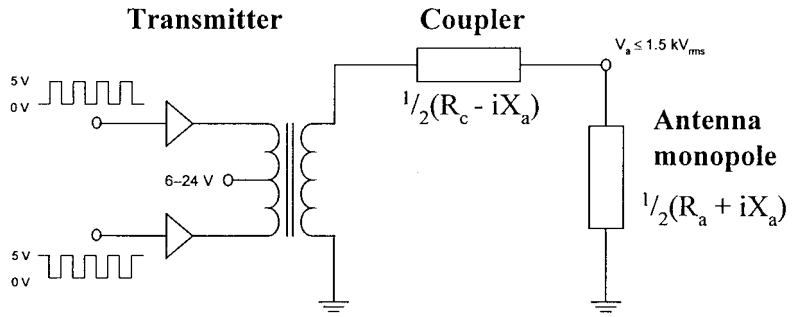


*Figure 9.* Equivalent circuit for one antenna element.

each half cycle of the radio frequency (RF). A simple step-up transformer would not improve efficiency. The solution adopted tunes the reactive elements in series with the antenna to cancel out the antenna's reactance. At low frequencies this element is simply an inductor whose reactance has the same magnitude as the antenna capacitance. Since they are opposite in sign, the reactive impedances cancel out, and the transmitter amplifier has to drive only the radiation resistance and ohmic loss resistances of the antenna and inductor. The resonating reactances actually store energy from one half cycle to the next, so the power to bring the antenna voltage up to 2 kV positive then 2 kV negative, does not all have to be supplied out of the amplifier each half cycle of the RF. The current into the antenna is equal to the current out of the amplifier, however, it is fed to the antenna at a higher voltage, therefore representing more power. Of course this power does not appear out of nowhere, it is simply swapped back and forth between the reactive components of the circuit, with only a small fraction of the energy being dissipated (radiation plus ohmic losses) each RF cycle. So the function of the resonant circuit is to produce a sufficiently high voltage that will radiate the desired power level.

It is not feasible to tune the inductor to each observation frequency. Instead, 14 different inductor values and 4 parallel capacitors at each step of inductance are combined to produce 108 discrete tuning steps in the band from 9.6–3000 kHz (Figure 11). The $Q$-factor of the tuner, $Q = |X_a|/R_c$, is sufficiently low so that the width of the tuned band at each step is sufficient to provide some overlap between steps, assuring continuous frequency coverage. Each coupler contains the L-C tuning elements for the monopole along with the control circuits for switching the relays (Figure 10).

*The transmitters.* The RPI creates the transmit pulses in the exciter circuits (Figure 10) using coherent local oscillator sine waves provided by the oscillator on the Analog1 card and the synthesizer on the DC1 card. The sinusoidal signals are gated by pulse signals from the timing circuits (Figure 6). These low voltage drive signals are sent to the four antenna couplers where they are amplified up to $\sim$ 75 $V_{\text{rms}}$ (variable, depending on frequency and power settings). This signal is then applied to the antenna wire, either directly or via the antenna tuners (Figure 11).

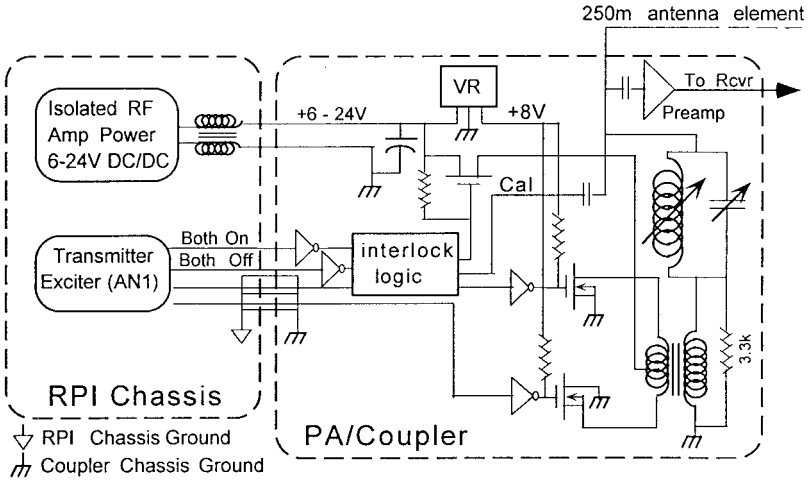


*Figure 10.* Power amplifier and antenna coupler. Low level voltage signals arrive from the transmitter exciter card in the main RPI chassis.

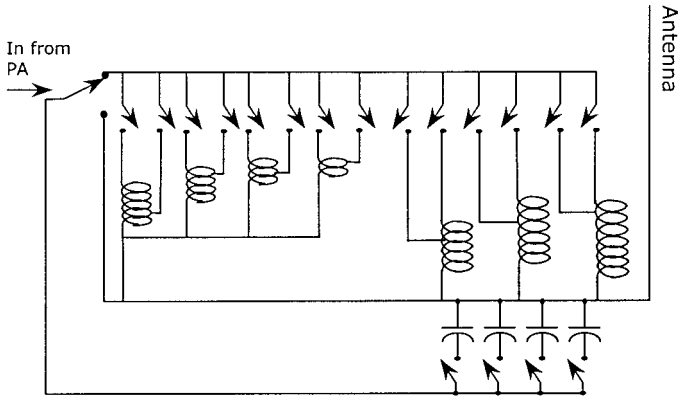


*Figure 11.* Switched antenna tuning for one antenna element. The switches are 5 kV relays.

Each of the four antenna coupler units contains a power amplifier which receives a logic level signal at the transmit frequency from the RPI electronics chassis. The amplifier consists of two power MOSFET transistors, which apply a square wave to the resonant circuit. The amplitude of the square wave is determined by the variable-voltage transmitter power supply, which feeds power to the MOSFET transistors. Conversion from square waves to sine waves is efficiently achieved by the tuned circuits.. The variable-voltage power supply is automatically controlled to limit $V_a$ to 1.5 $kV_{rms}$ and $P_r$ to 10 W. The transmitter power supply and amplifier were tested, as a function of frequency, by driving the current into an antenna simulator. The expected radiated power for one 250-m monopole was calculated from $P_r = I_a^2 R_r/2$ and is plotted in Figure 12.

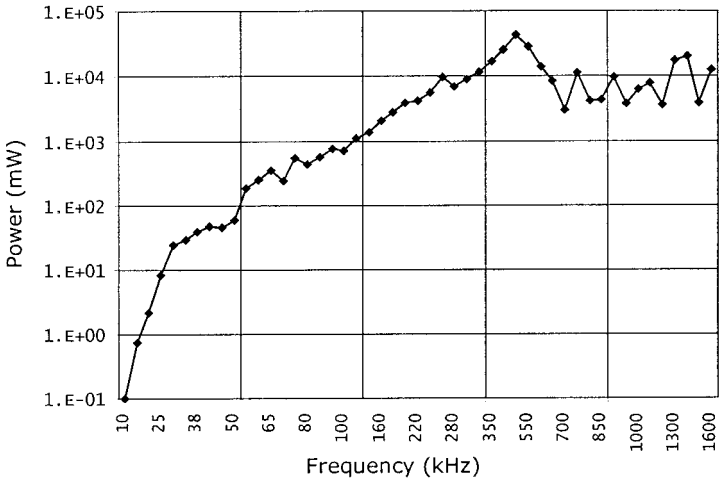


*Figure 12.* Measurement of radiated power per monopole. The peak near 500 kHz is caused by mistuning of the antenna simulator.

The commanding signals to the power transistors pass through some interlock logic, both for security and performance reasons. The selected voltage is applied to the transmitter MOSFETs only during a transmitter pulse. Also, there is a switch that detects the presence of an RF drive signal before power is applied to the transistors, since leaving the MOSFET gate at a high logic level with the voltage applied would short the power supply and cause it to shut down. Two lines control the MOSFET transistors: BOTH_ON and BOTH_OFF. BOTH_ON forces the MOSFETs to conduct, and automatically disables power while it is enabled. While BOTH_ON is enabled, the amplifier is a low impedance source and causes the tuned circuit to provide its maximum Q, during transmission.

With BOTH_OFF enabled, the MOSFETs are open and present a high impedance, which forces resonating currents into the damping resistor. This is called the quench pulse since it causes the coupler to quickly dissipates the stored energy. During pulse transmission, BOTH_ON and BOTH_OFF are disabled and the two power transistors are switched at the RF rate in a push-pull arrangement. The transformer, driven by the two transistors, steps up the power supply voltage by a factor of six, providing a maximum of 75 $V_{\text{rms}}$ to the tuned circuits. Finally, a detector circuit has been implemented which allows monitoring the voltage and current on the antenna. This monitoring verifies the level of the transmitted signal, and also helps determine that the antenna is properly tuned.

### 3.4. SIGNAL RECEPTION

The signals received on the antennas are amplified and impedance transformed in the wideband preamplifiers and sent to the receivers. The final intermediate

frequency signal at the receiver output is digitized and digital signal processing is applied depending on the operational mode.

*Preamplifiers.* Each of the six antenna elements drives a high-impedance, low-noise preamplifier included in the coupler boxes for the long-wire antennas. The preamplifiers have been designed to recover rapidly from the high voltage generated during the transmitter pulses. The antennas connect to the preamplifiers via small capacitors which, together with two clamping diodes (not shown in Figure 10), prevent the voltage at the amplifier input from exceeding the power supply levels. The preamplifiers for the 250-m monopoles have a gain of 8 dB and a noise level of about 7 nV/$\sqrt{\text{Hz}}$. The overall system sensitivity limit is about 8 nV/$\sqrt{\text{Hz}}$ for the $Z$ receiver and 25 nV/$\sqrt{\text{Hz}}$ for the X and Y receiver. The two $Z$ preamplifiers, which are mounted in a small box on the side of the z-axis antennas' deployment canister are similar to those in the couplers. They have the same noise levels as the X and Y preamplifiers; their gain can be switched between 12 and 24 dB.

*On-board calibration.* An attenuated derivative of the drive signal can be applied to the antenna via a small capacitance to perform self-calibration and to verify overall stability of the receiver system gain and phase. The calibration signal for the Z antenna receiver directly feeds the receiver and does not go through the preamplifiers.

*Receivers.* The frequency range for the RPI transmitters and receivers covers the range from 3 kHz to 3 MHz. The receiver bandwidth of 300 Hz is matched to the bandwidth of the transmitted waveform. This bandwidth provides a range resolution of 480 km with a range accuracy of 240 km or 480 km depending on the digitizer sampling rate described below. The gain of the preamplifiers helps to overcome noise picked up in the cables as the signal passes from the antennas to the X, Y and Z receivers located in the RPI main electronics unit. Since the $Z$ axis antenna is 25 times shorter than the X and Y antennas, at low frequencies (e.g., $<$ 100 kHz), the Z antenna receives a 25 times weaker signal which would provide a 28 dB weaker receiver output if not compensated for. Therefore the gain in the Z preamplifier is slightly higher than the X and Y preamplifiers, $+12$ dB compared to $+8$ dB, with a computer controlled optional setting of $+24$ dB. The Z receiver is designed with 15 to 20 dB more gain, making the options 19 dB to 36 dB more gain on the $z$ axis as compared to the $x$ and $y$ axes.

The RPI receivers are specially designed to be tolerant of the high-level transmitter pulse and to recover to full sensitivity within less than 7 ms (two reciprocal bandwidths). Since this is faster than the 'time constant' of the receiver would seem to allow, the special techniques employed should be explained. The most important aspect of this quick recovery from saturation is that a fixed gain is set before any pulses are transmitted, eliminating any consideration of an AGC (automatic gain control) response time, which would almost certainly be too slow for this application. The another important aspect of the design is that the receiver selectivity (i.e., the 300 Hz bandwidth) is not the result of a single reactive circuit, but is the

cascaded effect of 7 tuned stages of receiver IF, each with a bandwidth of 1 kHz. The tuning is performed with ferrite-loaded transformers and inductors, which are critically tuned based on the magnetic permeability of the ferrite core material. When a stage of the receiver is saturated, the currents are sufficient to depress the effective permeability of the tuned circuit in that stage. This core saturation detunes the stage thereby reducing the amplitude of the signal passed on to the next stage. During the transmitter pulse, all stages are bordering on saturation and it is important to discharge the tuned circuits as quickly as possible after the transmit pulse in order to receive echo signals. Each stage recovers with a time constant of roughly 1 ms.

By issuing VME commands over the VME backplane, the CPU can control the gain in six of the seven IF stages and one RF stage at the receiver front end. This design allows the receiver gain to be varied by 66 dB which, in addition to more than 60 dB of instantaneous dynamic range, gives an overall signal operating range of 126 dB (from 0 dBm to −126 dBm). At the −126 dBm (−139 dBV, or about 110 nV) end of the range, the sensitivity is increased further by the pulse compression and signal integration described later. Typical signal enhancement from signal processing is on the order of 20 dB, resulting in a system sensitivity of −146 dBm or about 12 $nV_{rms}$. The X and Y receivers provide about 12 dB less gain in the front end stage and achieve about 10 dB poorer sensitivity, or about 40 $nV_{rms}$ with signal processing gain. This processing gain should enable RPI to detect pulse echoes from ranges in excess of 5 Re (32 000 km).

The output of the X, Y and Z receivers is a 45 kHz IF signal, which is carried on the VME backplane to the Digitizer on the DC1 card. Here the signal is filtered again to isolate it from noise which might be picked up on the backplane. Then it is quadrature sampled at a rate of 625 Hz, or 1 sample each 1.6 ms. The sampling is triggered by the transmitter enable pulse, which ensures that the first samples received will be the saturated output of the receivers. This arrangement not only verifies that transmission took place but establishes the time origin for measuring the delay of echoes received. The digitized outputs are sent to a FIFO buffer where they are read into the CPU on the next 1.6 ms interrupt. The sample timing and occurrence of the interrupt are designed such that the all six, or three complex, receiver samples are finished and stable when the CPU tries to read them. This timing also guarantees that the FIFO buffer will never overflow. The CPU eliminates every other sample if the 480 km range increment has been chosen for the measurement, but the digitizer need not distinguish between the two settings. From this point, the CPU performs any signal processing and formatting as requested in the measurement program.

*Digital processing.* Quadrature sample records containing the desired echoes are made at each receiver output by the multichannel Digitizer and are processed by the CPU independently for each antenna. At the end of each frequency step the three processed records (one for each antenna) are passed to the CIDP. They retain the amplitude and phase information that is characteristic of the waves received

at each antenna. Depending on the selected measurement program and the data format, the CPU may process the echo data to improve the signal-to-noise ratio and compute Doppler spectra for each range. The format may output the entire Doppler spectra or may choose only a small part, but in all cases the data are separate for each antenna, allowing direction finding algorithms to be applied on the ground.

### 3.5. WAVEFORMS, SIGNAL PROCESSING AND GAINS

Because of the largely unknown magnitude of transport velocities of plasma structures or wave velocities in the magnetopause, the coherence and the Doppler characteristics of the expected RPI echoes can only be estimated. Therefore, RPI was designed with several waveforms of widely varying characteristics. The capability of the various waveforms is intimately related to the algorithms used to process the echo returns as explained below.

*Coherent integration.* The critical issue in selection of a waveform is the coherence time of the medium. The coherence time is the interval during which the phase of each of the sinusoidal components in an echo signal does not significantly change, that is, the complex amplitudes of successive samples of the same echo will sum in phase when accumulated over the integration period. If samples of a signal are not coherent then the mean amplitude of the accumulated sum of N samples will be larger than a single sample by the square root of $N$, which is the same increase as is achieved when integrating random noise. However, if the multiple samples are coherent, the amplitude of the accumulated sum is N times a single sample, which is root $N$ larger than the accumulated noise component of the signal, and therefore increases detectability, even for signals which are weaker than the received noise.

*Natural noise mitigation.* Natural noise, including auroral kilometric radiation (AKR) will interfere with the reception of weak echoes. Since the frequency spectrum of AKR noise is highly variable it will generally be possible to find quiet frequencies with low noise. A ‘frequency search’ technique is therefore used at each nominal sounding frequency just prior to the transmission of the pulse or the sequence of pulses. Five frequencies spaced by 300 Hz are tested around the nominal frequency, and the one with the lowest noise level is selected for sounding.

It would appear then that any Doppler shift large enough to change the phase of a signal by more than 90° during the integration would ruin the coherence. Spectral integration, however, corrects this phase shift for each resolvable Doppler frequency thereby allowing coherent integration for any signal that has a constant Doppler over the integration period. The characteristics that limit coherent integration time have to do with the extent to which the observed object is accelerating, since such acceleration leads to glinting, blinking or twinkling. The RPI instrument uses a variety of waveforms to ensure target detection in the presence of high Doppler shifts, acceleration or rapidly changing objects. The available waveforms and their mnemonic labels are listed in Table II.

TABLE II
RPI waveforms

| Mnemonic | Description |
|---|---|
| SHORT | Simple rectangular pulse of 3.2 ms pulsewidth which defines RPI's range resolution as 480 km (reciprocal of the 300 Hz receiver bandwidth) |
| COMP4 (or 8, or 16) | 4, 8 or 16 chip complimentary phase coded pulses with chip lengths of 3.2 ms. |
| CHIRP | FM chirp pulse provides high-gain pulse compression with single pulse. Can be repeated for spectral integration. |
| PLS125 (or 500) | 125 or 500 ms long pulse which provides a survey of Doppler shifts at the expense of range resolution. |
| SPS | Staggered pulse sequence, which consists of 212 pseudo-randomly spaced 3.2 ms pulses at each frequency to provide a maximum number of echoes within the limited coherence time of the medium. |

*Evenly spaced pulse sequences and their limitations.* To provide a detection range of 60 000 or 120 000 km requires a pulse repetition rate of 2 or 1 Hz, respectively, in order to avoid range aliasing. With such a slow repetition rate, several seconds are required to integrate repeated pulse transmissions. For instance, at 2 pulses per second the integration of 16 pulses, which provides a 12 dB signal-to-noise enhancement, would require 8 s of integration time. However, the medium may not be coherent over a period of several seconds, making it impossible to coherently integrate the received echoes. We have therefore provided the 16 chip complimentary phase code and the FM chirp waveforms which provide 12 and 18 dB of signal enhancement respectively within a single pulse period, which is 1 s or less. For science purposes, however, Doppler processing is desired to determine the radial velocity of the observed structures; also, as discussed in Section 1, Doppler separation aids the echo angle-of-arrival measurements.

Very fast moving structures, such as plasmoids and waves in the magnetopause, are estimated to produce tens of Hz Doppler shifts in the returned echoes. If the Doppler shift is greater than 1 Hz, while the pulse repetition rate is only 2 Hz, the Doppler shifted echoes will alias, i.e., fold-over, in the computed Doppler spectrum. The pulse repetition rate is equal to the data sampling rate, since for each range one data sample is obtained after each transmitted 3.2 ms pulse. If the echo frequency is shifted by tens of Hz, it becomes quite meaningless to produce a Doppler spectrum from the repeated pulse echoes. For such high Doppler conditions, the FM chirp pulse can be used to achieve a similar processing gain using only a single pulse. This single pulse technique does not, however, provide a Doppler spectrum.

TABLE III
Processing gains for different waveforms

| Waveform | Pulse compression | Spectral integration | Process gain [dB] | Max. velocity km $s^{-1}$ @ 30 kHz | Range coverage ($R_E$) |
|---|---|---|---|---|---|
| SHORT | No | Yes | 9 | 5 | 0.1–10 |
| COMP16[1] | Yes | Yes | 21 | 5 | 1.2–10 |
| CHIRP | Yes | No[2] | 18 | 750[3] | 2.4–8 |
| PLS125 | No | Yes | 20 | 750[3] | 1.5–10 |
| SPS | No | Yes | 21 | 750[3] | 0.1–19 |

[1] assuming 8 pulse repetitions at 2 Hz rate.
[2]Doppler integration can also be obtained by repeating chirp pulse $N$ times.
[3]300 Hz receiver bandwidth sets velocity limit.

*Long pulse.* To measure the true radial velocity of very fast moving plasma irregularities, RPI can use the long pulse waveform. The long pulse of either 125 ms or 500 ms duration is long enough to allow making a Doppler spectrum with a resolution somewhere between 2 and 8 Hz, and a Doppler range of $\pm 150$ Hz, limited only by the 300 Hz analog bandwidth of the receiver. Of course, these long pulses provide no useful range resolution. The Staggered Pulse Sequence (see below) provides the same Doppler range, but also provides range information with 480 km resolution. A summary of the available waveforms and their radar performance characteristics is given in Table III.

*Staggered pulse sequence.* Figure 13 depicts the staggered pulse sequence (SPS) in which short pulses are transmitted in a random pattern, and echoes from previously transmitted pulses are received in the listening time between transmissions. An echo received during a given listening time may have come from any of the preceding transmitted pulses, therefore the processing algorithm must provide discrimination of one range versus another. There is some inevitable leakage of energy from one range to the others, which would render the SPS waveform useless if, at any given frequency, more than about 30% of the ranges provide an echo. However, several factors tend to suppress echoes from range X while processing echoes from range Y:

– Samples for a given range are only accumulated into the ongoing Fourier integration if they correspond to a correct time delay since after a pulse is transmitted, others, corresponding to other time delays, are ignored.

– Echoes from the wrong ranges are sporadic impulses in the sampled data record; thus broadening their spectrum when spectrally integrated.

– A random phase shift is applied to the transmitted signals and is removed upon reception, so successive echoes will coherently integrate only for those echoes that result from the correct transmitted pulse, that is, those that experienced the time delay that corresponds to the range currently being processed.

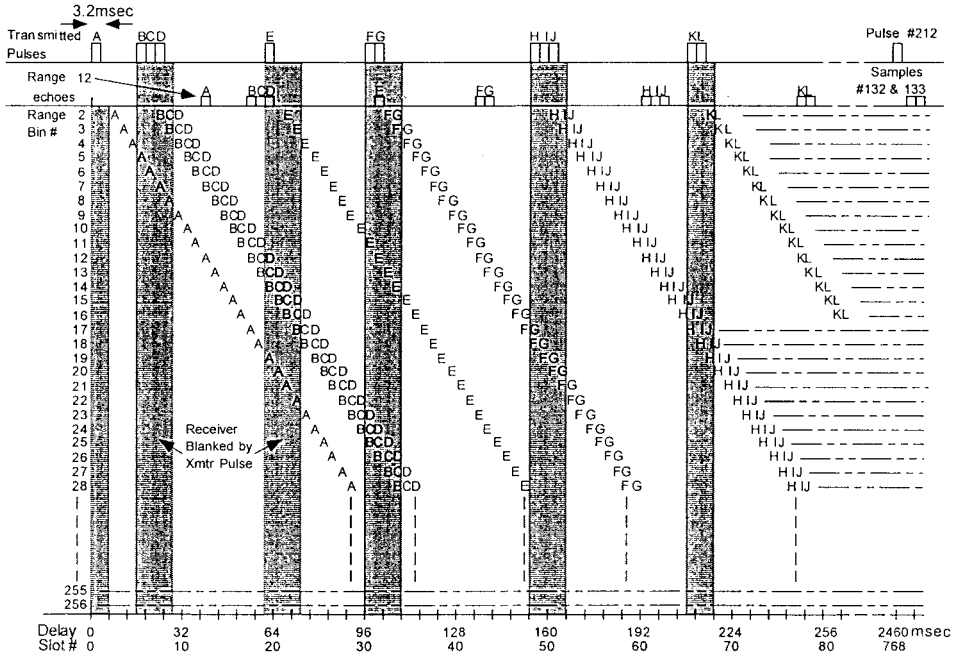


*Figure 13.* Staggered pulse sequence – Overlapping transmission and reception of pulse echoes.

Near the top of Figure 13 is shown an echo sequence received from a plasma surface at a range of 12 range bins, or 5760km. The echoes have a time delay associated with that range, and a phase, which indicates the radial velocity of the surface being observed. The determination of the Doppler shift, which provides the radial velocity measurement, is therefore a problem in the spectral analysis of non-uniformly spaced samples.

The ability to receive very weak echo signals at the same frequency and on the same antennas that just transmitted pulses of several kilovolts is made possible by the very fast quenching mechanism described in the hardware description of the antenna couplers. The RPI is able to recover full sensitivity in 3.2 ms, which is the time delay associated with just one resolvable range bin. This fast recovery is essential to the operation of the SPS waveform since there is a limited time between pulses during which received echoes can be sampled.

*FM Chirp.* The transmitted FM chirp waveform has an RF carrier that is linearly increasing in frequency (Barry, 1971) modulated by a rectangular pulse (Figure 14(a)). The chirp pulse waveform is characterized by its sweep rate ($\mathrm{d}f/\mathrm{d}t$) and pulse width. The resultant 244 Hz frequency sweep covered by the carrier during one pulse is insignificant in its effect on propagation or reflection characteristics of the structures being observed, and the limited frequency content also allows the pulse to be received within the fixed bandwidth of the RPI receiver. When an

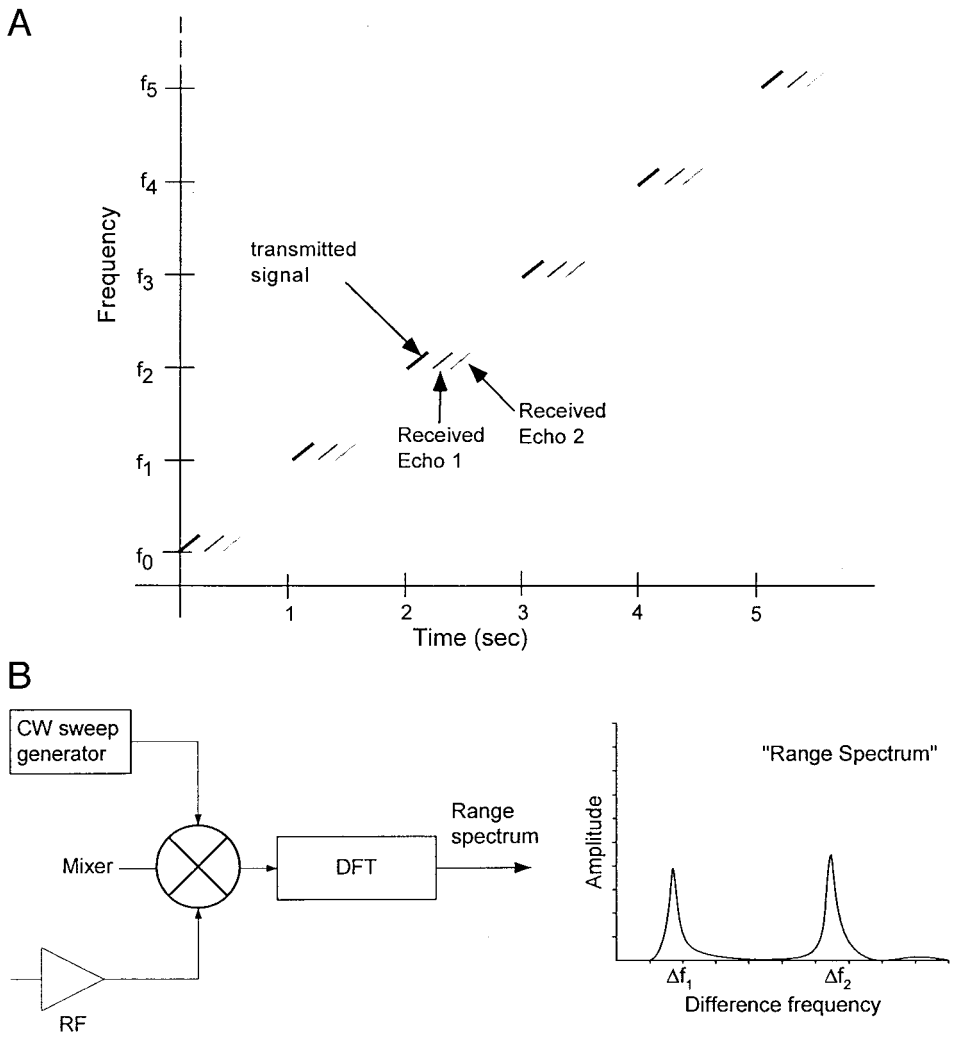


*Figure 14.* (a) Pulse chirp waveform and two echoes. The $f_i$ are the transmitter frequencies at the beginning of each new chirp pulse. (b) Receiver processing for chirp operation.

echo is received it is first mixed with a local oscillator signal which sweeps at the same rate used for the transmitted pulse (Figure 14(b)). Therefore the difference frequency generated in the mixer is a constant frequency that can be determined by Fourier analysis. This fixed frequency pulse has a duration equal to the transmitted pulse width (plus any time dispersion caused by the propagation medium) which gives it a spectral width that is inversely proportional to the pulse width. Since the oscillator frequency is known precisely, the difference frequency is linearly proportional to the time delay of the echo, and therefore directly represents the range to the object causing the reflection. A spectral analysis of the down-converted signal

produces a range profile of all echoes received (Poole, 1985). Since the receiver is linear, overlapping reception of multiple echoes from different ranges is resolved since they produce different Fourier component.

## 4. Measurement Programs and Schedules

At different parts of the IMAGE orbit RPI must be capable of measuring plasma densities that vary by six orders of magnitudes, velocities by four orders of magnitude, and signal powers by 12 orders of magnitude. To optimize the scientific output, it is therefore necessary to provide extreme flexibility in measurement programs and schedules. RPI will be pre-programmed to execute specific measuring programs on a cyclical schedule. The program scheduling procedure is illustrated in Figure 15. A 'Measurement Program' (MP) is specified by a set of 21 selectable control parameters. A total of 64 MPs can be stored and any one of them can be activated at a precise time by the active 'Program Schedule' (PS). The PS specifies the starting times of selected MPs with a 1 s resolution. While a total of 32 different PSs are stored, only one is activated at any given time. The PS that is valid at a given time is determined by a list of 256 'Schedule Starting Times' (SSTs). This procedure makes it possible to conduct very different combinations of measurements in different parts of the orbit and to vary the program sequences from orbit to orbit. The 64 MPs, 32 PSs and 256 SSTs require only 8,416 bytes and new MPs, PSs, or SSTs can be uploaded to the spacecraft whenever desired.

### 4.1. Measurement programs

Since the RPI operation is totally software controlled it is possible to create MPs that optimally adapt the RPI to the measurement objectives. One can create an MP by setting the 21 parameters listed in Table IV. They completely specify the operational mode, the measuring program, and the data storage format. The duration of a complete measurement covering the frequencies from ($L$) to ($U$) depends on the frequency step size and on the dwell time per frequency. This time can vary from less than 1 s to several minutes. The values listed in Table IV are stored together with the measured data in the data preface section of the RPI telemetry stream. A detailed description of the control parameters is given in the Data Format Document available from the authors. Convenient program-control panels with pull-down menus are provided for the operator to compose a MP. Their use is illustrated by discussing two MPs for different applications: DP-1 corresponds to a Doppler plasmagram measurement using one waveform (Figure 16(a)) and TM-1 corresponds to a thermal noise measurement (Figure 16(b)). The gray fields in the control panel indicate pull-down menus with precept values. The white fields indicate free choice of values, a pull-down menu contains some frequently used values. The settings of the control parameters are all stored together with the data.

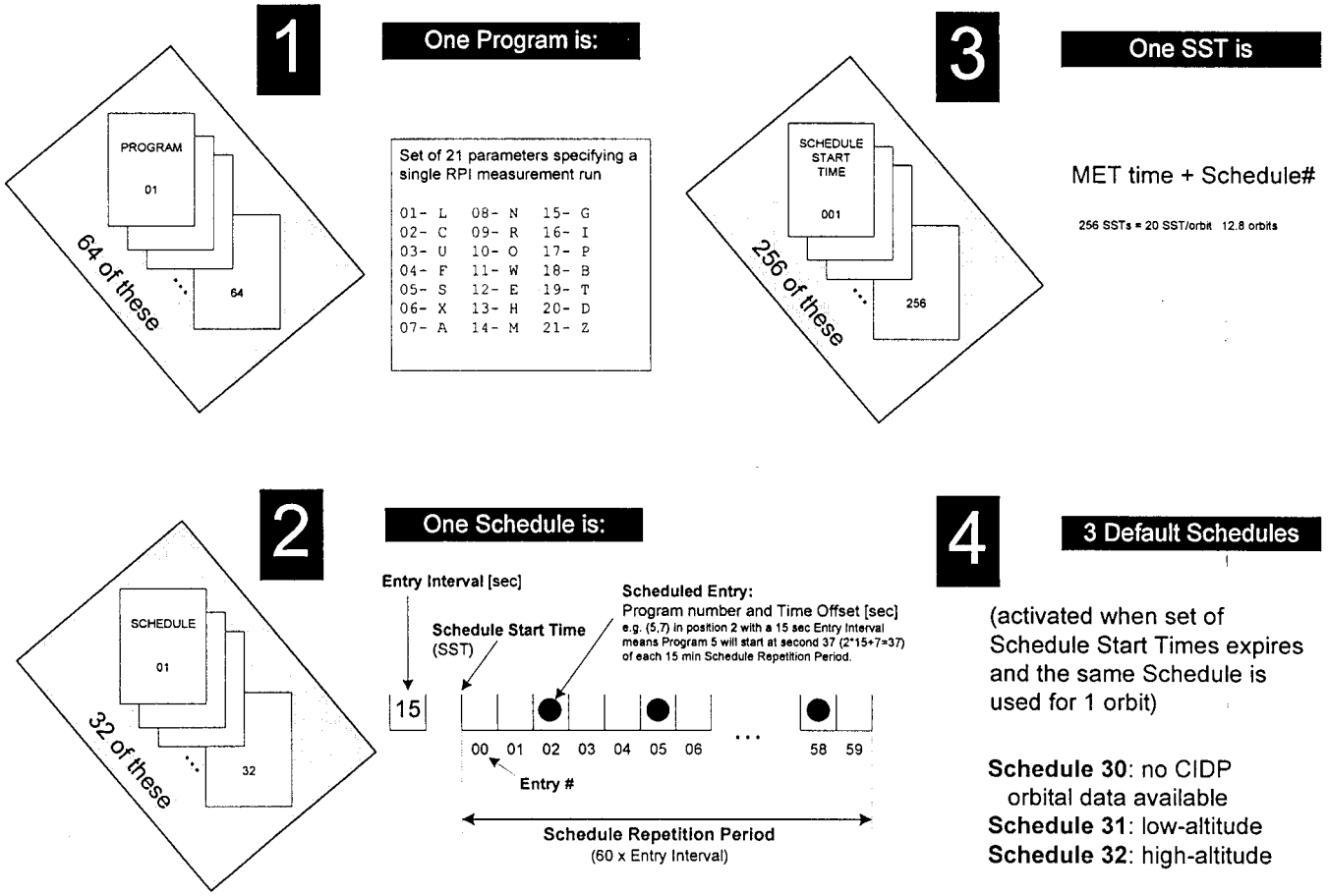


*Figure 15.* Measurement program and schedule structure.

TABLE IV
Measurement program parameters as stored in preface

| Item | Parameter | Units | Range of values | Default |
|---|---|---|---|---|
| 1 (L) | Lower frequency limit | kHz | 3 to 3000 | [10] |
| 2 (C) | Coarse frequency step/ | | | |
| | # of reps if (L)=(U) | %; 100 Hz if (C) < 0 | 1 to 100 (if%); −1 to −10,000 (if Hz)<br>1 to 255 (if repetitions) | [10] |
| 3 (U) | Upper frequency limit | kHz | 3 to 3000 | [100] |
| 4 (F) | Fine frequency step | 100 Hz | 1 to 10 000 | [1] |
| 5 (S) | # of fine steps | – | 1 to 8 (simultaneous integration)<br>−1 to −8 (same w/o multiplexing) | [1] |
| 6 (X) | TX waveform | X-table | 1 to 8<br>−1 to −8 (same w/o interpulse phase switching) | [1] |
| 7 (A) | Antenna configuration | A-table | 0 no transmission<br>1 to 8; −1 to −8 (antenna coupler bypassed) | [1] |
| 8 (N) | # of integrated repetitions, $2^N$ | – | 1 to 7<br>−1 to −7 (same but power integration instead of coherent integration) | [6] |
| 9 (R) | Pulse rep rate | $s^{-1}$ | 0, 1, 2, 4, 10, 20, 50 (0 means 0.5) | [2] |
| 10 (O) | Operating mode | O-table | C, R, S, T, W | [S] |
| 11 (W) | Instr. peak power limit | W | 0 to 100 | [0] |
| 12 (E) | First range | 960 km (2 × 3.2 ms) | 0 to 255 | [10] |
| 13 (H) | Range accuracy | km | 240 or 480 | [240] |
| 14 (M) | # of range bins | – | 8, 16, 32, 64, 128, 256, 512 | [256] |
| 15 (G) | Gain adjustment of receivers | 6 dB | 6 to 12 (automatic gain enabled)<br>0 to −12 (same but autogain disabled) | [9] |
| 16 (I) | Frequency spacing in clean-frequency search | 244 Hz | 0 no search<br>1 to 4 (searches 5 frequencies) | [0] |
| 17 (P) | # of archived ranges | – | 1 to 512 | [128] |
| 18 (B) | Bottom range tested | 960 km | 0 to 250 | [6] |
| 19 (T) | Top range tested | 960 km | 0 to 250 | [60] |
| 20 (D) | Data format | Table 5 | LTD, SSD, SMD, DBD, SBD, CAL, TTD | [0] |
| 21 (Z) | Data volume reduction | % | 0 to 99 | [0] |

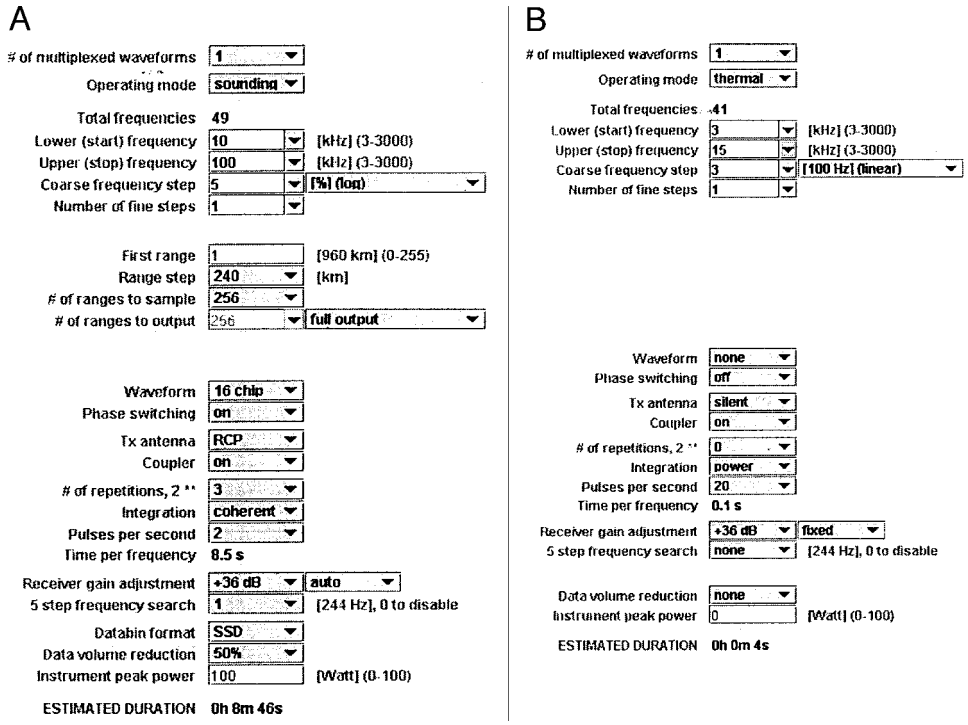


*Figure 16.* (a) Measurement Program DP-1. Sounding mode with complimentary phase code waveform. (b) Measurement Program TM-1: Thermal Noise mode.

When reading the archived data headers and prefaces, Table IV together with the respective sub-tables is used for interpretation.

The DP-1 program (Figure 16(a)) is designed for sounding in the magnetospheric cavity. The frequency scan is from 10 kHz to 100 kHz in 5% frequency steps. The value, 1, in the 'Number of fine steps' entry indicates that there are no fine steps used, and that the plasmagram is scanned in equal frequency steps of 5% as specified in the 'Coarse frequency step' entry. The echo ranges are sampled from 980 km to 62 180 km ($\sim$0.2 to 10 $R_E$) in 256 increments of 240 km. The 16-chip complimentary phase code waveform is used with interpulse phase switching, i.e., (X) $>$ 0 in Table IV., and coherent integration is applied. The transmission is right-hand-circular polarized (RCP) with regard to the $+z$-axis at full power; transmit antenna tuning is used (Coupler: on). The transmission on each frequency is repeated 8 times which makes it possible to generate an 8 line Doppler spectrum. At a pulse repetition rate of 2 Hz it takes 1 s to transmit one complimentary pair of pulses; for 8 repetitions the coherent integration time (CIT) becomes 8 s. Additional overhead time is required for antenna tuning and automatic gain setting. Data for all ranges are output to telemetry in SSD databin format (see Section 5), with 50% data volume reduction (the smallest 50% of the amplitudes are thresholded).

The thermal noise measurement program TM-1 (Figure 16(b)) is for a passive receive only spectral noise measurement scanning the receiver frequency from 3 kHz to 300 kHz in 300 Hz increments. One data sample (number of repetitions $= 2^{\circ} = 1$) for each antenna signal is recorded. In the thermal noise mode, the noise values for each frequency are the averages of 8 time samples spaced by 3.2 ms. The required time per frequency is 100 ms.

### 4.2. Measurement schedules

As shown in Figure 15, RPI can store up to 32 different Program Schedules (PSs). Only one PS is active at any given time. A PS contains 60 *entries*, where each entry can contain a MP number. The entries are spaced by $T$ seconds, where $T$, the *entry interval* can be specified from 1 s to 240 s. After the MP run listed in entry 60 is completed the MP listed in entry 1 will run next, unless a new PS is activated. The schedule repetition period varies from 1 min to 240 min (4 hours). The nominal starting times for entry #$x$ is $T(x - -1)$ seconds after schedule activation, but the actual starting time of any entry can be delayed by y seconds. The *offset time* $y$ is contained together with the MP # in each entry. A typical PS will usually have a number of unused entries because some MP runs will last several entry intervals.

### 4.3. Schedule initiation

To initiate a specific PS at a specified time it is necessary to specify the schedule start times (SST) and the PS number. RPI has a SST table with 256 entries that control which of the 32 PSs is active at any particular time. Each entry in the SST table contains the mission elapsed time (MET) and an PS number. The total storage requirement for the SST table is only 1280 bytes and it will be easy to uplink new SST tables on a weekly basis if necessary. This scheme allows up to 20 different PSs per orbit to be specified.

## 5. Data Formats and Browse Products

RPI's data architecture has adopted the concepts of the EOS Data and Information System (EOSDIS) (Rood and Stobie, 1993). The raw RPI data are collected at the IMAGE Science Mission Operations Center (SMOC) in the form of *Level 0* telemetry data packets. These, in turn, are processed at the SMOC to form higher-level products, including RPI browse products. The *Level 0.5* data, which presents the Level 0 RPI products in a commercial-strength standard format for telemetry data, uses the Universal Data Format (UDF) (Gurgioli, 2000). Level 0.5 distribution data and browse products for the whole mission are forwarded to the National Space Science Data Center (NSSDC) for further storage, retrieval and display. One of the NSSDC facilities, CDAWeb, will service Internet requests of RPI browse products.

### 5.1. LEVEL 0 DATA FORMATS

Level 0 comprises the raw data prepared by the RPI flight software for the downlink transfer. There are three basic types of Level 0 data produced by RPI: (1) time domain data, (2) spectral domain data, and (3) dynamic noise spectra. Time-domain data are the original 12-bit quadrature components sampled at each of the three antennas. The volume of time domain data collected by RPI may become quite large. For example, chirp sounding with 8 repetitions per frequency, 128 ranges and 140 frequencies results in $2\times$ (12-bit) $\times$ 3 antennas $\times 8 \times 128 \times 140 = 10.3$ Mbit of data. With up to 512 ranges, up to 128 pulses per frequency, two transmitter polarization modes and possibility of fine frequency stepping, RPI is capable of overflowing the RPI telemetry capacity for a number of orbits with a single measurement. Provisions were therefore implemented in RPI that allow onboard data reduction.

For pulse sounding modes, onboard coherent spectral integration of the time domain data will make data thresholding possible. Quadrature component pairs collected at the same frequency and range bin are Fourier transformed in the RPI CPU, resulting in a set of Doppler spectra (type 2 data) with 12 bit amplitudes and 12 bit phases. Because of the coherent integration, the Doppler spectra have a better signal-to-noise ratio and can be effectively cleaned by thresholding. Thresholded spectra yield a better ratio of onboard data compression performed by the spacecraft's CIDP. An additional saving of 33% in the data volume comes from reducing the 24-bit spectral data to 8-bit logarithmic amplitudes and 8-bit phase data. A more extreme data reduction can be accomplished by selecting and reporting only the spectral line with the maximum amplitude instead of the whole Doppler spectrum. In this case only one echo per range is allowed. Since all antenna data are reported individually it is still possible to determine the direction of the selected echo.

Another way to reduce the amount of telemetry data is to select and report only a part of the observed ranges by selecting the range interval with the strongest echoes. The subset of ranges to report is determined dynamically for each frequency as a fixed number of ranges in the vicinity of the strongest echo. The strongest echo can be searched in a specified section of all ranges between a 'Bottom' and a 'Top' range (see Table IV, items 18 and 19).

For all active RPI operating modes and processing options, we defined the minimum element of information, as a *databin*. All of the data collected are treated as a stream of databins, interspersed by some auxiliary information. Seven types of databins are defined in Table V.

At any operating frequency, the number of databins prepared for the downlink is known. It depends on the number of recorded ranges, the number of recorded Doppler lines per range (or repetitions, for the time domain data) and the number of polarizations used for transmission. The databins for each frequency are counted, lined up and preceded with a Frequency Header containing frequency, range of the first databin, antenna impedance data and some other auxiliary information.

TABLE V
Databin Types

| Databin type | Abbr. | Description |
|---|---|---|
| Linear time domain | LTD | Three 12 + 12 bit time domain quadrature components |
| Standard spectral domain | SSD | Three 8-bit log amplitudes and two 8-bit linear phases |
| Spectral maximum data | SMD | Three 8-bit log amplitudes, two 8-bit linear phases and one 8-bit Doppler shift |
| Double byte data | DBD | One 8-bit log amplitude and one 8-bit Doppler shift |
| Single byte data | SBD | One 5-bit log amplitude and one 3 bit Doppler shift |
| Calibration data | CAL | Three 8-bit log amplitudes, three 8-bit linear phases |

Then, the overall data stream is partitioned into fixed-sized packages. Each package contains a preface with MP-settings and a data header with MET (Mission Elapsed Time) offset from the nadir, total number of databins per frequency, and the serial number of the first databin in the package. This design ensures proper restoration of data in case of telemetry dropouts. For further details and a description of the data format for the dynamic noise spectra (type 3) we refer to the RPI Data Format Document (1999).

### 5.2. DATA DISPLAYS

A visual display of the RPI remote sensing data is complicated because the sounding data are multi-dimensional. Each amplitude value has associated with it information on phase, sounding frequency, Doppler frequency, echo range, angle-of-arrival, and wave polarization. Two complimentary browse products were developed for visual inspection of the sounding mode data that can provide the basis for scientific analysis: the *plasmagram* and the *echo-map*. For the display of thermal noise and noise emissions, a third browse product was developed, a dynamic noise spectrum.

*Plasmagrams*. The plasmagram gives the most complete visualization of the received signals in the sounding mode. It presents all signals received in a frequency-range frame. Figure 17 shows on the left side examples of simulated plasmagrams (Green et al., 1996) for the electron density profiles and satellite positions given on the right side. The plasmagrams have echo propagation delay time t in seconds on the vertical axis and sounder frequency $f$ in kiloHertz on the horizontal axis. For the magnetospheric model assumed in the simulation that produced Figure 17, only one echo is received at each sounding frequency. For the browse display (Figure 18) we chose the virtual echo range $R' = 0.5$ ct in Earth radii as vertical axis where c is the free-space speed of light. The individual echoes form traces with shapes that are reminiscent of ionogram traces. The variation of $R'(f)$ with frequency along

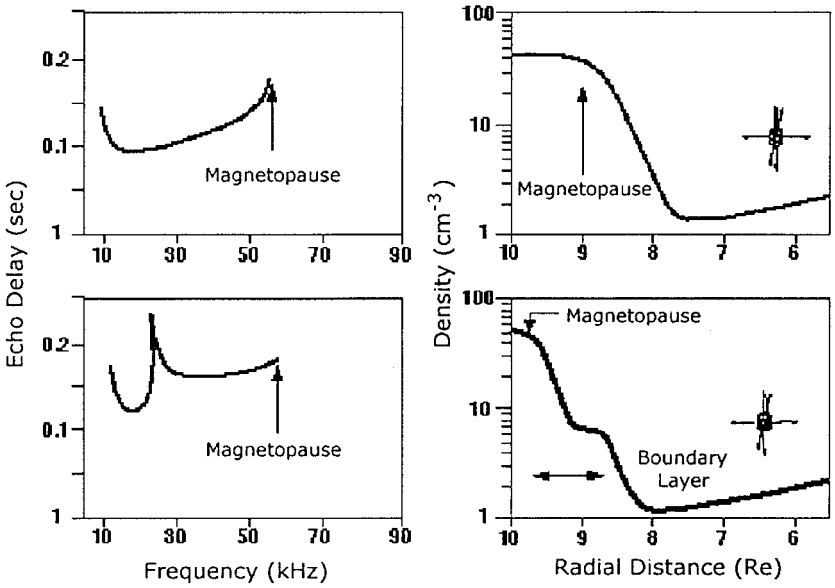


*Figure 17.* Simulated plasmagrams (left panels) and the magnetopause density profiles (right panels) without (top) and with a boundary layer (bottom) (after Green et al., 1996).

these traces gives an indication of the source of these echoes. The actual (or 'true') ranges $R(f)$ can be calculated from $R'(f)$ (Section 5.3).

The plasmagrams in Figure 17 give only a yes/no information for every frequency-range pixel indicating whether an echo signal is present. In this form, the plasmagram does not display other available information like amplitude, Doppler, polarization, and angle-of arrival, which are necessary to assess the 3-D plasma distribution in the magnetosphere. The plasmagram in Figure 18, on the other hand, was produced from bottomside ionogram data (Reinisch, 1996) to simulate an RPI Level 1 plasmagram browse product. It contains all the aforementioned additional information. Typically, the amplitude is represented as an optically weighted font (optifont) (Patenaude et al., 1973), and coarse Doppler and angle-of-arrival information is indicated by the color as explained in the figure caption. A collection of optifonts is available to display plasmagrams at different picture sizes.

For the purpose of creating the IMAGE Browse Products, all instruments present their images in a 'thumbnail' size to fit more of them on a single page or screen and thus provide means for a quick search of geophysical events. In the case of RPI, all Level 1 plasmagram data are transformed into a frame with fixed frequency and range scales, and color coded echo strength. This format makes it easy to follow the dynamics of magnetospheric $N_e$ structures. The thumbnail display provides a 'detail-on-demand' visualization strategy, where the full original scale plasmagrams can be invoked for closer analysis.

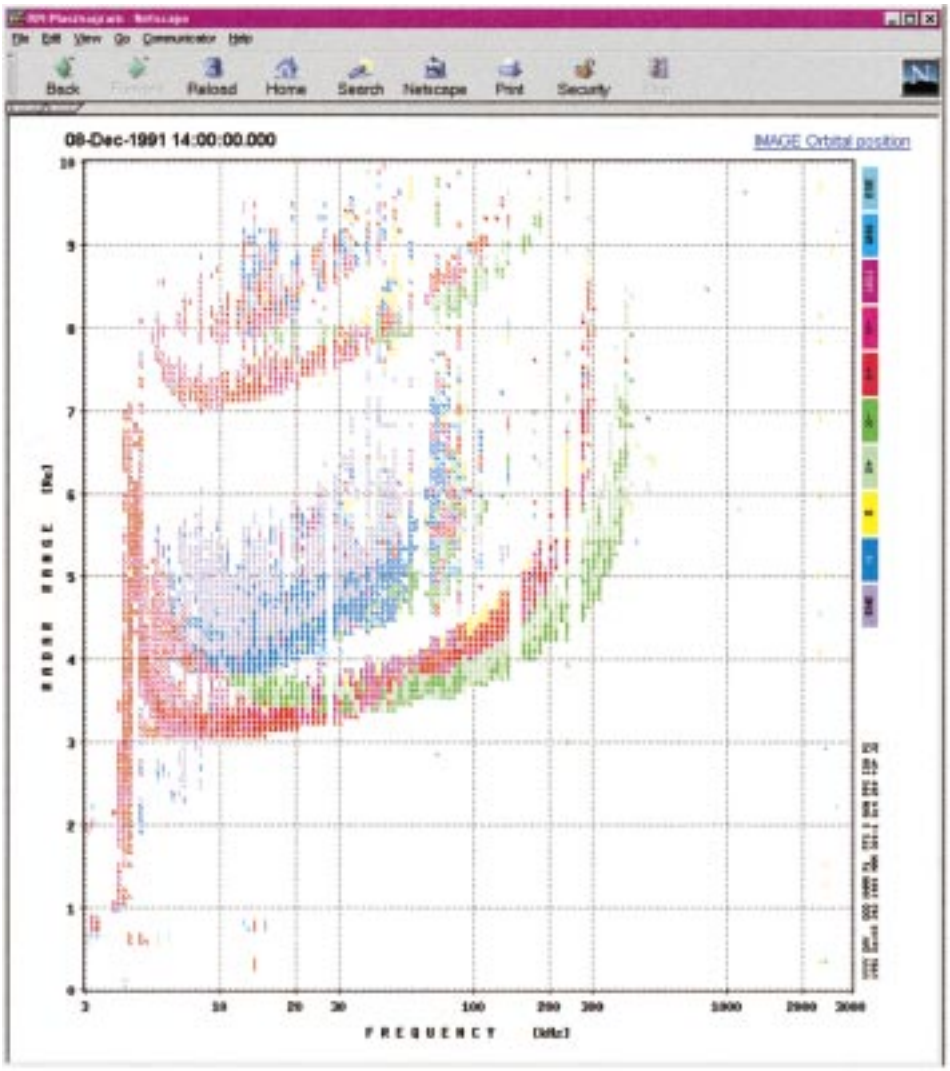


*Figure 18.* Detailed plasmagram frame displaying data from a digisonde ionogram. The amplitude display uses the 'optifont' that has increasing intensity with increasing value. The colors provide information on polarization, angle-of-arrival, and Doppler. All extraordinary echoes are printed in green (with two shades for positive and negative Doppler), vertical echoes in red (two shades), and off-vertical echoes are, N (dark blue), WNW (blue), WSW (brown), S (yellow), ESE (magenta), ENE (violet).

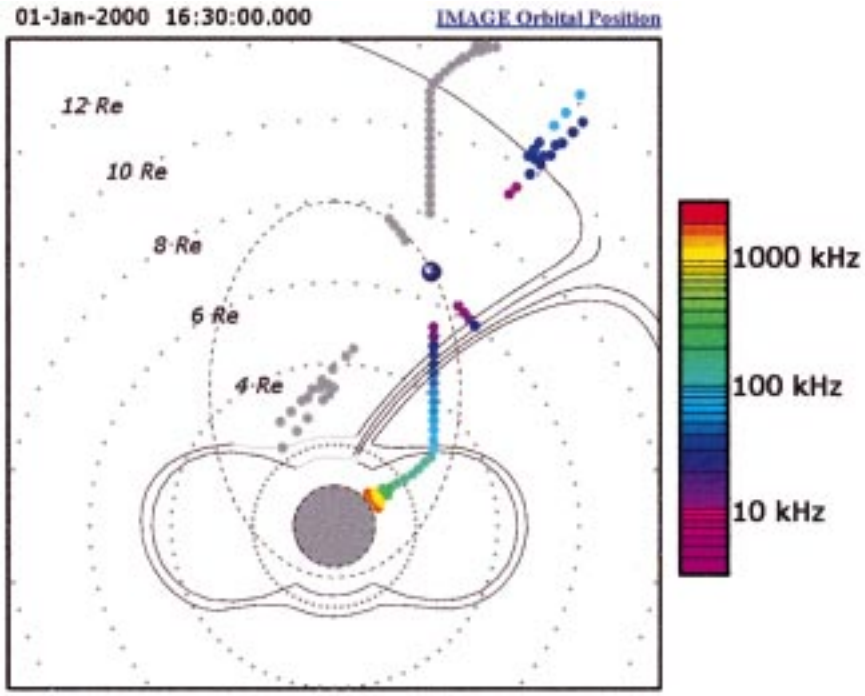


*Figure 19.* Detailed echo-map with superimposed magnetosphere, cusp and plasmasphere models. Color coding indicates the plasma frequency of the reflecting structure.

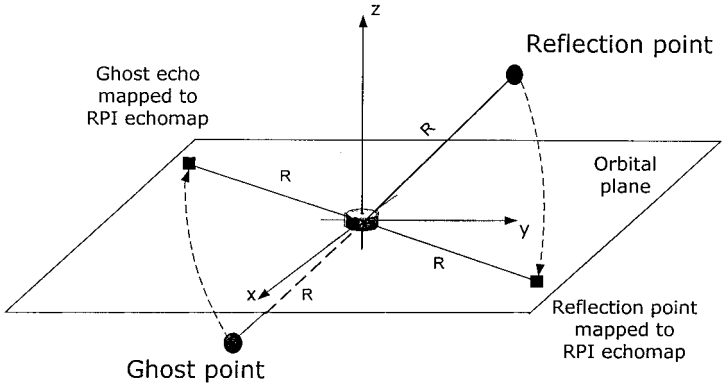


*Figure 20.* Mapping a reflection point onto the 2-D echo-map.

*Echo-maps*. An alternative way to present RPI sounding data is an echo-map (Figure 19), where the echo locations are projected into the orbital plane with a fixed layout of the Earth and the spacecraft orbit, and models of the magnetosphere and plasmasphere. The echo-map is a 2-D cross-section of the 3-D space, with all echoes projected onto it. The echo range is conserved by projecting each echo along into the echo-map as shown in Figure 20. Thus the echo locations on the 2-D plane

present both azimuth and range information. The colors of the echoes represent the sounding frequency, i.e., the plasma frequency of the reflecting structure.

Inherent in the construction of the echo-maps is the 180° ambiguity of the echo location as discussed in Section 2.1. On the echo-map, each echo is therefore accompanied by a *ghost* echo assumed to arrive from the opposite hemisphere. The browse display assumes one answer showing it in color but also shows the ghost location in gray. As pointed out in Section 2.1, this 180° ambiguity can be resolved by inspecting the plasmagram traces and comparing the deduced echo locations with predictions based on magnetospheric $N_e$ models.

*Dynamic noise spectra.* The browse product for the measured noise spectra are presented in two complimentary ways that are illustrated in Figures 21(a) and (b). Figure 21(a) shows one individual power spectrum as function of frequency, while Figure 21(b) shows a sequence of spectra as function of time for one complete orbit. Color coding is used to indicate the spectral power in Figure 21(b). The data are from Ulysses in the solar wind (Meyer-Vernet et al., 1998).

### 5.3. Electron density profiles

To assess the electron density distribution in the magnetosphere requires analysis of the plasmagrams and echo-maps. If an echo trace in the plasmagram is formed by echoes returning within a small angular cone it is possible to construct the $N(R)$ profile for the reflecting plasma structure from the $R'(f)$ measurements. $R'$ of an echo is larger than the true range, $R$, of the reflector from the spacecraft because the group velocity in the plasma is smaller than in free space. To find $R$ requires solving the integral equation (Jackson, 1969):

$$R'(f) = \int_0^{R(f)} \mu'[f; N_e(s), f_{\mathrm{He}}(s), \psi(s)]\, \mathrm{d}s \ . \tag{6}$$

Here $R'(f)$ is the virtual range of the O or X echo at the sounding frequency, f, and $\mu'$ is the corresponding group index of refraction (Huang and Reinisch, 1982), and $\psi$ is the wave normal angle defined in Figure 2. The functions $N_e(s)$, $f_{\mathrm{He}}(s)$ and $\psi(s)$ vary along the ray path from the spacecraft to the reflection point. Fortunately, dependence on $\mathrm{f_H}$ and $\psi$ is of second order and (10) can be evaluated with sufficient accuracy by using a model of the geomagnetic field. By applying the true range inversion algorithm of Huang and Reinisch (1982) to the simulated plasmagrams in the left panels of Figure 17 we were able to reconstruct the profiles on the right panels of that figure.

### 5.4. Wave polarization, characteristic waves and Faraday rotation

As discussed in Section 2, radio waves have elliptical polarization. The semiminor and semimajor axes a and b and the tilt angle $\tau$ in the $x'y'$ plane (Figure 3(b)) can

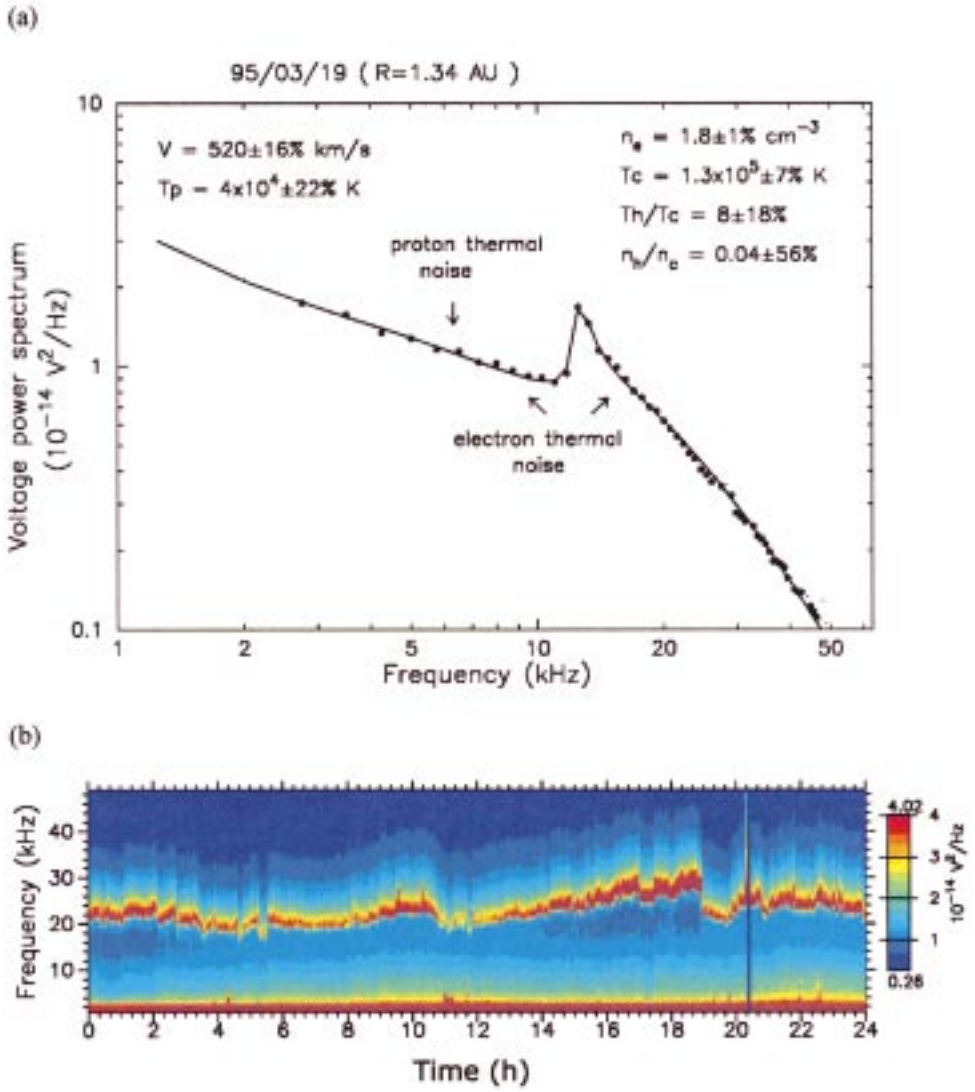


*Figure 21.* Thermal noise spectra. (a) Voltage power spectral density versus frequency. (b) Voltage power spectra versus time for a 24 h period. Ulysses data were used in this figure (Meyer-Vernet et al., 1998).

be determined from the quadrature samples of the signals at the three orthogonal antennas (Reinisch et al., 1999). To deduce the plasma density at the reflecting level we must know whether the received signal is an O- or an X-echo. This information can be obtained from the sense of rotation of the electric field vector. The polarization of the characteristic waves of frequency f at the spacecraft is totally determined by the local conditions, i.e., by $N_e$, $f_{pe}$, $f_{\mathrm{He}}$, and $\psi$. RPI will measure $f_{pe}$ and $f_{\mathrm{He}}$ in the relaxation mode, and $\psi$ can be estimated from models. It is

therefore possible to calculate the ratio of the semiminor and semimajor axes of the characteristic wave polarization. The sense of rotation is left-handed with respect to $\mathbf{B}_0$ (or its component along the wave normal) for the O-wave and right-handed for the X-wave (Rawer and Suchy, 1967, Section 7). As seen in many bottom and topside ionograms, and in simulated RPI plasmagrams (Green et al., 1999), both echoes arrive nearly simultaneously for some frequencies and the measured field will be the sum of the two characteristic waves, i.e. the O- and X-wave. Reinisch et al. (1999) have shown that the measured polarization ellipse can be decomposed into the O- and X- ellipses and the semimajor axes $a_o$ and $a_x$ determined. The sense of rotation of the composite ellipse depends on whether $a_o/a_x$ is larger or smaller than 1. If it is larger than 1, the $\mathbf{E}_R$ field vector rotates like an ordinary wave and vice versa (Kelso, 1964, Ch. 2).

When the O- and X-waves travel together, the composite polarization ellipse will change its tilt angle, $\tau$ (Figure 3(b)) progressively, the well-known Faraday rotation (Yeh et al., 1999). Reinisch et al. (1999) have estimated the total Faraday rotation, $\tau_F$, for typical echoes expected for the RPI measurements to be $\sim 19\pi$ which cannot be directly measured. They proposed to measure the differential rotation between two frequencies spaced by $\sim$0.5% which is of order $0.1\pi$ and therefore measurable. Using some approximations described by Davies (1990, Ch. 8), they derived the differential rotation as:

$$\Delta\tau_F(f) = -\frac{2\Delta f}{f}\tau_F \approx -\frac{2\pi\,\Delta f}{cf^2}\int_0^R f_{pe}^2(s)\, f_{He}(s)\cos\psi(s)\,\mathrm{d}s\ . \tag{7}$$

The value for the integral can be obtained from the $\Delta\tau_F$ measurements. The integral can, however, also be directly calculated using the $N(R)$ profile that was calculated using a $\mathbf{B}_0$ model. Comparing the results of these two independent methods will provide a check of the accuracy of RPI's $N(R)$ profiles and the $\mathbf{B}_0$ models used.

## 6. Summary

The RPI on IMAGE is a versatile plasma wave instrument capable of conducting remote and *in situ* measurements of magnetospheric plasma densities. The extreme flexibility of selecting the measurement program parameters will optimize the data collection for the different parts of the elliptical spacecraft orbit. In active sounding measurement runs, RPI will receive echoes from the magnetopause, the plasmasphere, the cusp, and even the ionosphere. Angle-of-arrival and wave polarization measurements for a sequence of frequencies will allow the determination of the electron density distribution in the magnetosphere. These measurements will be made using three orthogonal receive antennas and applying quadrature sampling

techniques. While short 3.2 ms pulses will be used for echo sounding, a long 500 ms pulse will be used to trigger whistler-mode propagation.

In passive measurement runs, RPI will measure the local electron density and temperature using quasi-thermal noise spectroscopy. Data from the long 500-m tip-to-tip spin plane antennas will be used around apogee in the magnetospheric cavity, and from the orthogonal 20-m antenna near perigee in the plasmasphere. Data from all three antennas will be used to measure the intensity and angle-of-arrival of natural radio emissions.

## Acknowledgements

This research was supported by NASA subcontracts 83822 to UML and 83814 to Raytheon ITSS from SwRI, and by NASA contract NASW-97002 to Raytheon ITSS. The authors would like to acknowledge the excellent efforts put forth by the members of the RPI team who made it possible to design, build and test the RPI instrument, most notably: Stephen Stelmash, Kevin Roche, and Jason Grochmal from the University of Massachusetts Lowell; Scott Allen, Carl Devillier, Larry Howe and Gary Heinemann from AEC-Able Engineering Company, Inc. Last but not least we thank Jim Burch and Bill Gibson of Southwest Research Institute and their staff for excellent cooperation, and Barry Birdwell for providing the seamless interface.

## References

Barry, G. H.: 1971, 'A Low-Power Vertical-Incidence Ionosonde', *IEEE Trans.* **GE-9**, 86–95.

Bibl, K. and Reinisch, B. W.: 1978, 'The Universal Digital Ionosonde', *Radio Sci.* **13**, 519–530.

Bougeret, J.-L., Kaiser, M. L., Kellogg, P. J., Manning, R., Goetz, K., Monson, S. J., Monge, N., Friel, L., Meetre, C. A., Perche, C., Sitruik, L. and Hoang, S.: 1995, 'Waves: The Radio and Plasma Wave Investigation on the WIND Spacecraft', *Space Sci. Rev.* **71**, 231–263.

Calvert, W., Benson, R. F., Carpenter, D. L., Fung, S. F., Gallagher, D. L., Green, J. L., Haines, D. M., Reiff, P. H., Reinisch, B. W., Smith, M. F. and Taylor, W. W. L.: 1995, 'The Feasibility of Radio Sounding in the Magnetosphere', *Radio Sci.* **30** (5), 1577–1595.

*Data Format Document for the Radio Plasma Imager*: 1999, Center for Atmospheric Research, University of Massachusetts Lowell, 900 Suffolk Street, Lowell, MA.

Davies, K.: 1990, *Ionospheric Radio*, Chapt. 8, Peter Peregrinus Ltd., London, U.K.

Fung, S. F. and Green, J. L.: 1996, 'Global Imaging and Radio Remote Sensing of the Magnetosphere, Radiation Belts Models and Standards', *Geophysical Monogr.* **97**, AGU, Washington, D. C., 285–290.

Green, J. L., Fung, S. F. and Burch, J. L.: 1996, 'Application of Magnetospheric Imaging Techniques to Global Substorm Dynamics', *Proc. Third International Conference on Substorms (ICS-3)*, Versailles, France, ESA SP-389, pp. 655–661.

Green, J. L., Taylor, W. W. L., Fung, S. F., Benson, R. F., Calvert, W., Reinisch, B. W., Gallagher, D. L. and Reiff, P. H.: 1998, 'Radio Remote Sensing of Magnetospheric Plasmas, Measurement Techniques in Space Plasma: Fields', *Geophys. Monogr.* **103**, AGU, Washington, D. C., 193–198.

Green, J. L. et al.: 2000, 'Radio Plasma Imager Measurements', *Space Sci. Rev.* **91**, 361–389 (this issue)

Gurgiolo, C.: 2000, 'The IMAGE High-Resolution Data Set', *Space Sci. Rev.* **91**, 461–481 (this issue)

Gurnett, D. A., Persoon, A. M., Randall, R. F., Odem, D. L., Remington, S. L., Averkamp, T. F., Debower, M. M., Hospodarsky, G. B., Huff, R. L., Kirchner, D. L., Mitchell, M. A., Pham, B. T., Phillips, J. R., Schintler, W. J., Sheyko, P. and Tomash, D. R.: 1995, 'The POLAR Plasma Wave Instrument', *Space Sci. Rev.* **71**, 597–622.

Hald, A.: 1962, *Statistical Theory with Engineering Applications*, Chapt. 5, J. Wiley, New York.

Huang, X. and Reinisch, B. W.: 1982, 'Automatic Calculation of Electron Density Profiles from Digital Ionograms. 2. True Height Inversion of Topside Ionograms With the Profile-Fitting Method', *Radio Sci.* **17** (4), 837–844.

Issautier, K., Meyer-Vernet, N., Moncuquet, M. and Hoang, S.: 1999, 'Quasi-Thermal Noise in a Drifting Plasma: Theory and Application to Solar Wind Diagnostic on *Ulysses*', *J. Geophys. Res.* (in press).

Jackson, J. E.: 1969, 'The Reduction of Topside Ionograms from the Bottomside and Topside', *J. Atmos. Terr. Phys.* **27**, 917–941.

Kelso, J. M.: 1964, *Radio Ray Propagation in the Ionosphere*, Chapt. 2, McGraw-Hill, New York.

Kraus, J. D.: 1988, *Antennas*, Ch. 5, McGraw Hill, New York.

Lund, E. J., Labelle, J. and Treumann, R. A.: 1995, 'On Quasi-Thermal Noise Fluctuations Near the Plasma Frequency on the Outer Plasmasphere: A Case Study', *J. Geophys. Res.* **99**, 23,651–23,659.

Meyer-Vernet, N. and Perche, C.: 1989, 'Toolkit for Antennae and Thermal Noise Near the Plasma Frequency', *J. Geophys. Res.* **94**, 2405.

Meyer-Vernet, N., Hoang, S. and Moncuquet, M.: 1993, 'Bernstein Waves in the Io Torus: a Novel Kind of Electron Temperature Sensor', *J. Geophys. Res.* **98**, 21,163–21,176.

Meyer-Vernet, N., Moncuquet, M. and Hoang, S.: 1995, 'Temperature Inversion in the Io Plasma Torus', *Icarus* **116**, 202–213.

Meyer-Vernet, N., Hoang, S., Issautier, K., Maksimovic, M., Manning, R., Moncuquet, M. and Stone, R.: 1998, 'Measuring Plasma Parameters with Thermal Noise Spectroscopy', in E. Borovsky and R. Pfaff (eds), *Geophysical Monograph 103: Measurements techniques in Space Plasmas*, pp. 205–210.

Moncuquet, M., Meyer-Vernet, N., Bougeret, J. L., Manning, R., Perche, C. and Kaiser, M. L.: 1995, 'WIND Passes Through the Outer Plasmasphere: Plasma Diagnosis from the Quasi-Thermal Noise Spectrum Measured by the Waves Experiment', *Supp. to Eos* **76**, 17, 221.

Patenaude, J., Bibl, K. and Reinisch, B. W.: 1973, 'Direct Digital Graphics, the Display of Large Data Fields', *American Laboratory*, pp. 95–101.

Poole, A. W. V.: 1985, 'Advanced Sounding 1, the FMCW Alternative', *Radio Sci.* **20**, 1609–1620.

Rawer, K. and Suchy, K.: 1967, 'Radio Observations of the Ionosphere, in S. Flügge (ed.), *Encyclopedia of Physics*, XLIX/2, Geophysics III/2, Sect. 7, Springer-Verlag, Berlin.

Reinisch, B. W., Buchau, J. and Weber, E. J.: 1987, 'Digital Ionosonde Observations of the Polar Cap F Region Convection', *Physica Scripta* **36**, 372–377.

Reinisch, B. W.: 1996, 'Modern Ionosondes, in Modern Ionospheric Science', in H. Kohl, R. Rüster and K. Schlegel (eds), *European Geophysical Society*, 37191 Katlenburg-Lindau, ProduServ GmbH Verlagsserie, Berlin, Germany, pp. 440–458.

Reinisch, B. W., Haines, D. M., Bibl, K., Galkin, I., Huang, X., Kitrosser, D. F., Sales, G. S. and Scali, J. L.: 1997, 'Ionospheric Sounding in Support of OTH Radar', *Radio Sci.* **32**(4), 1681–1694.

Reinisch, B. W., Sales, G. S., Haines, D. M., Fung, S. F. and Taylor, W. W. L.: 1999, 'Radio Wave Active Doppler Imaging of Space Plasma Structures: Angle-of-Arrival, Wave Polarization, and Faraday Rotation Measurements with RPI', *Radio Sci.* **34** (6), 1513–1524.

Rood, R. B. and Stobie, J. G.: 1993, 'Data Assimilation and EOSDIS', *NASA Internal Report*.
Shawhan, S. D.: 1970, 'The Use of Multiple Receivers to Measure the Wave Characteristics of Very-Low-Frequency Noise in Space', *Space Sci. Rev.* **10**, 689–736.
Yeh, K. C., Chao, H. Y. and Lin, K. H.: 1999, 'A Study of the Generalized Faraday Effect in Several Media', *Radio Sci.* **34**(1), 139–153.